Title

Age-specific and compartment-dependent changes in mitochondrial homeostasis and cytoplasmic viscosity in mouse peripheral neurons

James N. Sleigh[1,2]*, Francesca Mattedi[3,4]*, Sandy Richter[3,5]*, Kristal Ng[3]†, I. Emilie Steinmark[6]†, Iveta Ivanova[6]†, István L. Darabán[3], Parth P. Joshi[3,7], Emily Annuario[3], Shirwa Awale[6], Gokhan Yahioglu[8], Jacqueline C. Mitchell[3], Klaus Suhling[6], Giampietro Schiavo[1,2], Alessio Vagnoni[3]‡

[1]Department of Neuromuscular Diseases and UCL Queen Square Motor Neuron Disease Centre, UCL Queen Square Institute of Neurology, University College London, London, UK.

[2]UK Dementia Research Institute, University College London, London, UK.

[3]Department of Basic and Clinical Neurosciences, Maurice Wohl Clinical Neuroscience Institute, Institute of Psychiatry, Psychology and Neuroscience, King's College London, London, UK.

[4]Current address: Department of Neuromuscular Diseases, UCL Queen Square Institute of Neurology, University College London, London, UK.

[5]Current address: Department of Biomedical Sciences, University of Padova, Padova, Italy.

[6]Department of Physics, King's College London, Strand, London, UK.

[7]Current address: Sunderland Medical School, University of Sunderland, UK.

[8]Antikor Biopharma Ltd, Stevenage Bioscience Catalyst, Stevenage, UK.

‡ Corresponding author: alessio.vagnoni@kcl.ac.uk

*These authors contributed equally

†These authors contributed equally

Abstract

Mitochondria are dynamic bioenergetic hubs that become compromised with age. In neurons, declining mitochondrial axonal transport has been associated with reduced cellular health. However, it is still unclear to what extent the decline of mitochondrial transport and function observed during ageing are coupled, and if somal and axonal mitochondria display compartment-specific features that make them more susceptible to the ageing process. It is also not known whether the biophysical state of the cytoplasm, thought to affect many cellular functions, changes with age to impact mitochondrial trafficking and homeostasis. Focusing on the mouse peripheral nervous system, we show that age-dependent decline in mitochondrial trafficking is accompanied by reduction of mitochondrial membrane potential and intra-mitochondrial viscosity, but not calcium buffering, in both somal and axonal mitochondria. Intriguingly, we observe a specific increase in cytoplasmic viscosity in the cell body, where mitochondria are most polarised, which correlates with decreased cytoplasmic diffusiveness. Our work provides a reference for studying the relationship between neuronal mitochondrial homeostasis and the viscoelasticity of the cytoplasm in a compartment-dependent manner during ageing.

Introduction

Ensuring precise distribution and functionality of mitochondria is essential for maintaining cellular homeostasis. The complex architecture and long distances between nerve terminals and soma of neurons cause these cells to be highly dependent on mechanisms for long-range cytoskeletal transport of mitochondria and on continuous mitochondrial supply and functionality along their extended cellular architecture. This is a particularly critical challenge for neurons, which are post-mitotic

and can live throughout the adult life of an organism. It is therefore not surprising that mitochondrial dysfunction is a recognised hallmark of ageing and neurodegeneration [1].

We have previously shown that axonal transport of mitochondria decreases in the peripheral nervous system of ageing *Drosophila melanogaster* [2] and that neuronal ageing phenotypes, such as oxidative stress and focal protein accumulation, can be manipulated by modulation of mitochondrial transport [2,3]. Mitochondrial motility was shown to be downregulated during ageing to varying degrees also in *C. elegans* motor neurons and in the mouse central nervous system neurons *in vivo* [4–6]. Despite the consistent observation that mitochondrial trafficking is slowed down during ageing, it remains unclear whether this directly correlates with the functional changes in mitochondria during ageing.

The biophysical properties of the neuronal cytoplasm are under increasing scrutiny in the context of neurodegeneration [7,8], although the effect of age on these properties is less well studied. Whether fundamental properties of the neuroplasm, such as viscosity and diffusion, undergo significant changes that can affect intracellular cargo trafficking and functionality during ageing is currently unknown.

A study that combines the analyses of the motile behaviour of neuronal cargoes and their functional state with the evaluation of the biophysical properties of the cytoplasm in young and old neurons has been lacking, partly due to lack of suitable experimental systems to perform this type of study and the challenge of studying these processes in live neurons throughout ageing. Interrogating cellular processes in animal models

in vivo is indispensable for ageing studies, although gaining mechanistic insight can be a challenge in this context [9]. For example, neuronal cells *in situ* often have their soma, axons and dendrites embedded in different tissues and organs and so studying functional compartmentalisation *in vivo* becomes challenging. In an ageing context, being able to complement *in vivo* studies with a species-specific *in vitro* model of neuronal ageing would be particularly advantageous.

In this study, by focusing on the mouse peripheral nervous system, we filled this gap through comparative analyses of mitochondrial trafficking in dorsal root ganglion (DRG) neurons *in vitro* and sciatic nerve axons *in vivo* from both young and aged mice. Using the DRG model, we also monitored other important aspects of mitochondrial biology within neurons, including mitochondrial membrane potential, calcium uptake and intra-mitochondrial viscosity, and we revealed age- and compartment-dependent alterations in these properties. We expanded on these data by quantifying intracellular viscosity and diffusion in the neuronal cytoplasm of the somal and axonal compartments and propose a novel model that correlates mitochondrial homeostasis with the viscoelasticity of the neuronal cytoplasm during ageing.

Results

Mitochondrial trafficking declines with age in mouse peripheral neurons both *in vitro* and *in vivo*

To better characterise the effect of ageing on mitochondrial trafficking in mouse peripheral neurons, we isolated and cultured sensory neurons from DRG of young (3-4 months) and old (19-22 months) mice (Fig. 1A), and analysed mitochondrial axonal transport by live imaging with MitoTracker. DRG neurons grow robustly in culture after

dissection, retain their age-dependent transcriptional profile [10] and have previously been used to study axonal cargo trafficking during ageing [11,12]. Time-lapse recording and quantification of mitochondrial axonal transport showed abundant mitochondrial movement in both the anterograde and retrograde directions, with a small proportion of mitochondria displaying bidirectional motility (Fig. 1B-C, Fig. S1) [11,13–15]. Neurons obtained from old mice showed a strong reduction in the percentage of moving mitochondria (Fig. 1B-C, Fig. S1), but no significant change in the number of mitochondria present in the axons (Fig. 1D). Moreover, the speed and displacement of these organelles were largely unaffected by age, both in the anterograde (Fig. 1E) and retrograde directions (Fig. 1F).

To assess whether the age-dependent decline in mitochondrial transport observed in cultured DRGs was preserved in peripheral neurons *in vivo*, we analysed mitochondrial axonal transport in intact sciatic nerve axons of anaesthetised MitoMice (Fig. 2A), in which neuronal mitochondria are marked by cyan fluorescent protein (CFP) (Fig. 2B-C and Movie 1) [16]. Old mice displayed a clear reduction in mitochondrial motility (Fig. 2D and Movie 1), which was accompanied by a decrease in the overall number of axonal mitochondria (Fig. 2E). When the proportion of mitochondrial motility was assessed, no difference between young and old neurons was identified (Fig. S2A) in either anterograde or retrograde directions (Fig. S2B). This indicates that the decline in the number of motile mitochondria is not due to a net change in the proportion of moving mitochondria, rather a general decrease in mitochondrial axonal content, which may be linked with an imbalance in mitochondrial biogenesis and/or turnover. While the motile properties of the retrograde-moving mitochondria remained unchanged with age (Fig. 2G), the speeds and displacement of the fewer anterograde-

moving mitochondria were surprisingly upregulated in older mice (Fig. 2F), contrasting with what observed in cultured DRG neurons. Interestingly, the distributions of mitochondrial speed and displacement measured in the sciatic nerve and cultured neurons were significantly different (Fig. 1E-F, 2F-G, and Table S1), potentially indicating a different regulation of the molecular motor machinery *in vivo* and *in vitro*. Overall, these data show that mitochondrial axonal trafficking is affected by age in peripheral nerves both *in vitro* and *in vivo*, although the underlying mechanisms may differ in the two systems.

Mitochondrial membrane potential is compartment-dependent and decreases with age and declining mitochondrial viscosity

To understand if the trafficking defects are associated with altered mitochondrial functionality, we first asked whether the membrane potential ($\Delta\Psi_m$) of these organelles was altered between young and old DRG neurons. We stained the neurons with a low concentration of the live dye tetramethylrhodamine methyl ester (TMRM), which accumulates in active mitochondria, as well as MitoTracker Green (MTG) to label all mitochondria (Fig. 3A-D). Calculating the ratio of TMRM to MTG fluorescence has previously been used to determine mitochondrial membrane potential in live cells, where a higher ratio indicates more polarised mitochondria [17]. Using this method here reveals that the membrane potential of neuronal mitochondria decreases with age (Fig. 3E and Fig. S3A-B) and that the axonal compartment is characterised by mitochondria with substantially lower membrane potential, independently of age (Fig. 3F-G).

It is possible that decreased trafficking and altered membrane potential during ageing are mechanistically linked, although the two phenotypes could also manifest independently. To test if decreased mitochondrial trafficking has a direct effect on membrane potential in DRGs, we used an RNAi construct to reduce the abundance of Trak1, which is essential to drive mitochondrial motility in the axons [18]. Trak1 knockdown in young DRG neurons reduced mitochondrial transport (Fig. S3C) but had no impact on membrane potential (Fig. S3D-F). This indicates that acute reduction of mitochondrial axonal transport does not directly affect $\Delta\Psi_m$, suggesting that the two phenotypes in the aged neurons are not mechanistically linked. Nevertheless, we cannot exclude that chronic reduction of mitochondrial transport during ageing or a time-specific reduction in older neurons could have a knock-on effect on the maintenance of $\Delta\Psi_m$.

Manipulations that decrease mitochondrial membrane potential have been shown to affect the viscosity of these organelles in HeLa and COS7 cells [19–22], while altered mitochondrial membrane viscosity has been observed in human AD brains [23] and murine neurons during neurodegeneration and ageing [24,25]. We therefore asked if the age-dependent changes in $\Delta\Psi_m$ that we observe in DRGs might be accompanied by changes in the viscosity of the mitochondria. To do so, we performed fluorescence lifetime imaging microscopy (FLIM) of neurons incubated with the BODIPY-based fluorescent molecular rotor FMR-1 targeted to the mitochondrial matrix (Fig. 3H) [20]. Fluorescence lifetime of FMR-1 responds to changes in viscosity environments, where a longer fluorescence lifetime indicates higher viscosity [20]. Neuronal mitochondria display a heterogeneous viscosity profile both in the cell bodies and axons (Figure 3H), in accordance with previous work carried out in HeLa and COS7 cells [19,20]. Similar

to $\Delta\Psi_m$, average mitochondrial viscosity decreases during ageing as indicated by decreased lifetime (Fig. 3I and Fig. S3G-H). In this case, however, the viscosity of the mitochondria remains largely unchanged between the cell bodies and axons in both young and old neurons (Fig. 3J-K). These results suggest that while the striking difference in $\Delta\Psi_m$ between somal and axonal mitochondria is unlikely to be coupled to organelle viscosity (as this remains constant across compartments), the decline of $\Delta\Psi_m$ and mitochondrial viscosity during age may be linked.

Ca^{2+} buffering is unaffected in DRG neurons cultured from young and old mice

Loss of $\Delta\Psi_m$ has long been thought to negatively affect Ca^{2+} accumulation in mitochondria [26,27] and, in mouse sensory neurons, $[Ca^{2+}]_m$ uptake causes a transient loss of $\Delta\Psi_m$ [27]. Increased mitochondrial viscosity was also suggested to correlate with augmented cytosolic calcium in HeLa cells [20]. We therefore asked whether the age-dependent changes in the $\Delta\Psi_m$ and mitochondrial viscosity are accompanied by alterations in $[Ca^{2+}]_m$ uptake. We depolarised DRG cultures by transient stimulation with 50 mM KCl and measured the fluorescent signal of mitochondrial and cytosolic Ca^{2+} using the Rhod-2-AM and Fluo4-AM dyes, respectively [27,28] (Fig. 4A-D). Combined measurements from both the somal and axonal compartments showed that there was no overall difference in the timing and abundance of mitochondrial Ca^{2+} uptake (Rhod-2-AM) between young and old cells (Fig. 4E,G). Likewise, we did not detect any significant difference in the increase of cytoplasmic Ca^{2+} abundance (Fluo4-AM) elicited by neuronal stimulation between young and old neurons (Fig. 4F,H). Taken together, these data show that age does not affect Ca^{2+} homeostasis in cultured DRGs.

Age-dependent increase in cytoplasmic viscosity is inversely correlated with diffusiveness in neuronal cell bodies but not in axons

Previous studies have shown that hypertonic treatments, which acutely increase molecular crowding and cytoplasmic viscosity, affect cytoskeletal dynamics in fission yeast [29], alter ER-to-Golgi transport in COS7 cells [30] and abolish endosomal motility in mammalian immune cells [31]. To test whether decreased mitochondrial transport in ageing DRG neurons correlates with a change in fluid-phase viscosity of the cytoplasm, we performed time-resolved fluorescence anisotropy imaging (TR-FAIM, Fig. 5A) [32,33]. TR-FAIM measures the depolarisation of fluorescence emission of a dye (fluorescein derivative 2′,7′-bis-(2-carboxyethyl)-carboxyfluorescein, BCECF) caused by rotational Brownian motion, and so it is used to obtain information about the viscosity of the cellular microenvironment [34]. Anisotropy decay measurements and fitting (Fig. S4A and see Methods) showed that the rotational correlation time of the dye is significantly reduced in older cells leading to slower depolarisation (Fig. 5B), which is indicative of higher cytoplasmic viscosity in old DRGs (Fig. 5C). Because of the specialised architecture of neurons, we hypothesised that the somal and axonal compartments might comprise different viscosity environments. Measurement of the anisotropy decay in cell bodies and axons revealed that, although the two compartments have similar viscosity values in young cells (Fig. 5D, F and Fig. S4B), the viscosity of the cell bodies undergoes a significant increase in aged cells (Fig. 5E-F and Fig. S4C-D), whereas the axonal viscosity remains unchanged during age (Fig. 5D-F and Fig. S4B-C, E). These results suggest that axonal viscosity alone is unlikely to explain the observed decrease in mitochondrial axonal transport.

Fluid-phase viscosity affects the diffusiveness of the cytoplasmic milieu, as determined by the Stokes-Einstein law [35]. To gain more insight into cytoplasmic diffusiveness in our *in vitro* cell model of ageing, we performed rheological studies by measuring the diffusion rates of genetically-encoded multimeric nanoparticles (GEMs) [36]. GEMs can be visualised as bright spherical particles of uniform shape and size that are suitable for microrheological studies in different cellular contexts [29,36,37]. We transduced DRGs with a lentiviral vector encoding sapphire-tagged GEMs of 40 nm diameter (Fig. 6A, D) and tracked particle movement in cell bodies and axons (Fig. 6B-C, E-F and Movie 2-3). Single particle tracking and MSD analysis showed that GEM movement is consistent with sub-diffusive motion (Fig. 6G and Fig. S5A), in accordance with previous reports in non-neuronal cell types [29,36]. In both young and old neurons, the diffusion rate of axonal GEMs is significantly lower than the rate of GEMs freely diffusing in cell bodies (Fig. 6G-I and Fig. S5), suggesting that the specialised axonal architecture poses a significant physical constraint for particle diffusion. The diffusion of somal GEMs is reduced in aged cultures (Fig. 6G-I), in accordance with the observed increase in viscosity. Interestingly, although the axonal viscosity does not change during ageing (Fig. 5D-F, Fig. S4B-C, E), GEMs display a small, albeit significant, reduction in diffusiveness in aged culture (Fig. 6G-I), indicating that mechanisms other than viscosity regulate axonal diffusion during ageing.

Based on these experiments, we conclude that the behaviour of cytoplasmic fluid-phase viscosity during ageing is defined by the cellular compartment, with a potentially distinct effects on somal and axonal biology. Indeed, while increased viscosity likely contributes to reduced cytoplasmic diffusion in the neuronal cell bodies, axonal

viscosity is not a driver of the decreased diffusiveness of the axonal cytoplasm nor of the reduced active mitochondrial axonal transport during ageing.

DISCUSSION

In this study, we monitored fundamental mitochondrial and cytoplasmic properties in peripheral neurons of young and aged mice; we find that decreased mitochondrial axonal trafficking correlates with changes in mitochondrial membrane potential and mitochondrial viscosity as well as with changes in cytoplasmic viscosity and diffusiveness that are affected by age in a compartment-dependent manner (Fig. 7).

Altered mitochondrial axonal trafficking is an established feature of ageing peripheral neurons in *Drosophila* and *C. elegans in vivo* [2,4] and of mouse sciatic nerve *ex vivo* [38]. We now show that the number of motile axonal mitochondria declines both in aged DRG neurons *in vitro* and in the sciatic nerve *in situ* (Fig. 7), although the underpinning mechanisms are likely to be different. The total number of axonal mitochondria remains stable *in vitro* showing that decreased transport may not be sufficient to determine the steady-state distribution of mitochondria in axons, as previously suggested [2,38]. On the other hand, decreased mitochondrial motility in the sciatic nerve of older mice may be coupled to impairment in biogenesis or mitochondrial clearance that could lead to an overall reduced number of axonal mitochondria.

Decreased mitochondrial motility is accompanied by a surprising increase in the processivity of anterograde mitochondria in aged neurons *in vivo*. It is possible this is a compensatory mechanism triggered by age, similar to upregulation of cargo trafficking observed in response to peripheral nerve injury [38,39]. This result is interesting

as it shows that the decline in mitochondrial motility during ageing can be partly reversed in mammalian neurons, as demonstrated previously in ageing *Drosophila* neurons [3]. Understanding the mechanisms behind the transport upregulation in older neurons might therefore be of therapeutic interest for age-dependent neurodegeneration when decline in cargo trafficking can play an important role in disease progression [40,41].

Decline in mitochondrial functionality is an active focus of research in the ageing field [42,43] with mitochondrial oxidative stress [44] and mitophagy [45–47] thought to play a potentially critical role during ageing. The observation that the $\Delta\Psi_m$ decreases in aged DRG neurons (Fig. 7) implies that the mitochondria become overall less functional and is consistent with reduced mitochondrial bioenergetics observed in iNeurons derived from old human donors [48]. Upregulation of retrograde transport of dysfunctional mitochondria with reduced $\Delta\Psi_m$ was observed in murine hippocampal [15] and chicken DRG neurons [49] suggesting this could be a mechanism for recycling of dysfunctional mitochondrial in the cell soma. We now show that this potential safeguarding mechanism may be impaired during ageing due to a strong reduction in mitochondrial motility in both the anterograde and retrograde directions. Interestingly, we find that the mitochondria that reside in the cell body are much more polarised than axonal mitochondria and this is observed independently of age. These results suggest that single axonal mitochondria may be metabolically less active than the those found in the interconnected mitochondrial network within the cell body. Alternatively, axonal mitochondria might be more prone to damage, possibly due to a reduced turnover in the axon, where basal mitophagy may occur at different rates than in the cell body [50], or impaired fission and fusion dynamics as a result of decreased trafficking. Whatever

the case, our observations support the idea of a mitochondrial functional gradient along the axons whereby mitochondria become progressively less active as the distance from the cell body increases [51,52].

Reduced $\Delta\Psi_m$ is accompanied by an overall reduction in the intramitochondrial viscosity in aged DRG (Fig. 7), which could conceivably reflect an adaptation to metabolic activity [53,54] that becomes altered with age. Alternatively, decreased molecular crowding within the mitochondria [55] or changes in their membrane fluidity as a result of oxidative damage [23,25] could explain reduced viscosity. Interestingly, protein diffusion was shown to be enhanced in mitochondria of human fibroblasts that are deficient for complex I activity [56], likely a sign of reduced viscosity, while mitochondria hyperpolarisation correlates with increased viscosity in HepG2 cells [55]. Thus, our data support the idea that the reduced $\Delta\Psi_m$ and mitochondrial viscosity in aged DRGs are mechanistically linked.

Contrarily to $\Delta\Psi_m$, however, mitochondrial viscosity across compartments remained uniform, which suggests independent mechanisms might regulate $\Delta\Psi_m$ and viscosity in different compartments. Mitochondrial viscosity was shown to be selectively unaffected by acute osmotic stress compared to other organelles [19]. Therefore, it is possible that mitochondrial viscosity is less sensitive to stressors that could determine a difference in $\Delta\Psi_m$ across compartments. Overall, our study adds significantly to the notion of mitochondrial functional specialisation that has been observed across different neuronal populations [57] and within subcellular compartments [58]. Future studies should be aimed at further characterising the mitochondrial microviscosity

environment to assess whether sub-mitochondrial domains are differently affected by age in different cellular compartments.

Acute increase in cytoplasmic calcium levels can suppress mitochondrial motility [59,60] and the calcium content of mitochondria has been correlated with their motile behaviour [61,62]. Interestingly, we find that even though mitochondria are overall less polarised in aged DRG cultures when their motility declines, this does not affect their capacity to buffer calcium or the wider neuronal excitability in this context (Fig. 7). Thus, it is conceivable that the population of healthy mitochondria in the older DRG neurons is sufficient to compensate for the dysfunctional organelles, although we cannot exclude that the calcium uptake capability is retained in depolarised organelles.

Whether cytoplasmic viscosity and diffusion undergo significant changes during ageing that can affect intracellular trafficking is not known. Previous studies showed that increased viscosity reduces both endosomal trafficking and microtubule dynamics [29,31]. Changes in cytoplasmic viscosity are thought to depend on alterations of molecular crowding, with likely repercussions on wider cellular functionality [63–66]. Using TR-FAIM, we find that axonal cytoplasmic viscosity does not change with age and so it is unlikely to have a major impact on the biology of the axon, including the decrease in mitochondrial motility that we observe in older DRG neurons (Fig. 7). However, we find that, contrarily to axons, the viscosity of the cell bodies increases in aged cultures. Why cell bodies selectively display increased viscosity is not clear. This could result from an imbalance in protein translation [36], a potential temperature difference across compartments as the cell ages [53], for example as a consequence of reduced metabolic activity [67], or be the product of compartment-dependent difference in plasma

membrane viscosity and stiffness [68–70]. Whatever the case, it is conceivable that the stark increase in the cytoplasmic viscosity of the cell soma is sufficient to impact mitochondrial dynamics, including mitochondrial export into the axon, and wider cellular functionality in aged cells.

We find that the molecular diffusion in the neuronal cytoplasm, ascertained using the GEM probe, decreases with age in both soma and axons (Fig. 7). While this is consistent with the increased viscosity of the cell soma, it seems apparently at odds with the constant axonal viscosity measured by TR-FAIM. However, our data are in accordance with the notion that macromolecular crowding in complex cellular environments can cause deviation from the Stokes-Einstein law that relates diffusion and viscosity [71]. Therefore, we speculate that older axons may develop proteinaceous aggregates and/or molecular condensates that, while not sufficient to alter overall viscosity, can provide significant spatial hindrance by increasing local crowding in small calibre DRG axons. This could explain both the slower diffusion of the 40 nm GEM particles and the well documented decrease in organelle motility observed during ageing and neurodegeneration. In future studies, it would be valuable to determine whether local viscosity and diffusion in proximal and distal axonal regions display different rates, and to establish if this is a general feature of the nervous system or confined to a specific subset of neurons. Ultimately, it would be relevant to understand whether age-dependent neurodegenerative diseases are characterised by specific viscosity and diffusion patterns and whether this could be exploited to model disease progression.

Overall, our study uncovers new aspects of mitochondrial homeostasis and cytoplasmic biophysics in aged neurons (Fig. 7). This work will provide an important reference for future studies aimed at better understanding mitochondrial functionality and the role of the cytoplasmic milieu for cellular homeostasis.

ACKNOWLEDGEMENTS

We thank personnel of the Denny Brown Laboratory for assistance with mouse colonies, Gábor Mórotz for suggestions regarding calcium imaging experimental setup, BFK Lab for assistance with MSD analyses, the Wohl Cellular Imaging Centre at King's College London for help with light microscopy, Frank Hirth and members of the Vagnoni lab for comments on the manuscript. Fig. 1A, 2A and 7 were created using https://www.biorender.com. This project was funded by a NC3Rs David Sainsbury Fellowship NC/N001753/2 and SKT grant NC/T001224/1 (to A.V.), a BBSRC CTP award BB/T508597/1 (to A.V.), Royal Society Research Grant RGS\R2\180450 (to A.V.), an Academy of Medical Sciences Springboard Award SBF004/1088 (to A.V.), a van Geest Fellowship in Dementia and Neurodegeneration and van Geest PhD studentship awards (to A.V.), a King's Together Multi and Interdisciplinary Research Scheme Wellcome Trust Institutional Strategic Support Fund 204823/Z/16/Z (to A.V.), and by the Alzheimer's Research UK London Network Centre grant ARUK-NC2020-KCL, a BBSRC award BB/R004803/1 (to K.S.), a Medical Research Council award MR/S006990/1 (to J.N.S.), a Wellcome Trust Sir Henry Wellcome Postdoctoral Fellowship 103191/A/13/Z (to J.N.S.), Wellcome Trust awards 107116/Z/15/Z and 223022/Z/21/Z (to G.S.), and a UK Dementia Research Institute Foundation award UKDRI-1005 (to G.S.). D.S. and I.E.S. were supported by a BSCB Studentship and a LIDo iCASE Studentship, respectively.

For the purposes of open access, the author has applied a Creative Commons Attribution (CC BY) licence to any Accepted Author Manuscript version arising from this submission.

MATERIALS AND METHODS

Study approval

Experimentation involving mice was performed under license from the UK Home Office in accordance with the Animals (Scientific Procedures) Act (1986). Work conducted at University College London was approved by the Queen Square Institute of Neurology Ethical Review Committee and experiments performed at King's College London were approved by King's College Denmark Hill Ethical Review Body.

Animals

Mice were maintained under a 12 h light/dark cycle at constant room temperature (≈21°C) with free access to water and food. Cages were enriched with nesting material, plastic/cardboard tubes and wooden chew sticks. MitoMice (B6.Cg-Tg(Thy1-CFP/COX8A)S2Lich/J – RRID:IMSR_JAX:007967) were obtained from The Jackson Laboratory and maintained as hemizygous × wild-type breeding pairs on a C57BL/6J background. Presence of the CFP transgene was confirmed by a standard condition polymerase chain reaction using forward primer 5'- GAC GTA AAC GGC CAC AAG TT-3' and reverse primer 5'- GTC CTC CTT GAA GTC GAT GC-3'. C57BL/6J wild-type mice were obtained from Charles River Laboratories UK Ltd. Mice of both sexes were used in all experiments. DRGs obtained from MitoMice were used for live imaging of mitochondrial transport and Ca^{2+} imaging experiments, while DRGs from C57BL/6J mice were used for live imaging of mitochondrial membrane potential and mitochondrial viscosity, TR-FAIM and microrheology experiments. Young and old cells were imaged in the same or in contemporary experimental sessions, whenever possible, rather than 20 months apart.

DRG dissection and culture

DRGs were dissected from the spinal cord of euthanised adult mice [72]. Approximately 10 DRG pairs (*i.e.*, 20 DRG) were collected for each mouse, and kept on ice in Ca^{2+}/Mg^{2+}-free HBSS with 1% Pen/Strep until dissociation. DRGs were cultured as previously described [73]; briefly, after removing the HBSS, the DRGs were incubated in 4 mg/ml collagenase type II (Thermo Fischer Scientific #17101015) and 4.67 mg/ml dispase type II (Sigma-Aldrich #D4693) in Ca^{2+}/Mg^{2+}-free HBSS at 37°C for 10-15 min with periodic gentle agitation. The collagenase/dispase solution was replaced with pre-warmed F12 media (F12 (Gibco) containing 10% heat-inactivated-FBS (hi-FBS) and 1% Pen/Strep (both from Thermo Fischer Scientific)). Upon centrifugation, cells were resuspended in F12 media and triturated using fire-polished glass Pasteur pipettes. After centrifugation at 200 *g* for 5 min, cells were resuspended in 320 μl of fresh DRG media (F12, 10% hi-FBS, 1% Pen/Strep, 20 ng/ml mouse GDNF (Peprotech #450-44), 50 ng/ml mouse NGF (Peprotech #450-34), 20 ng/ml human NT3 (Peprotech #450-03)) and plated as single 20 μl drops (1-2 drops/well or coverslip) at 37°C, 5% CO_2 for 1-2 h. 0.3-1 ml of DRG media was then gently added to each well and cells were returned to the incubator. Cells were plated in μ-Slide 8-well glass bottom imaging chambers (Ibidi #80827), in 8- and 4-well Nunc Lab-Tek chambered coverglass (Thermo Fischer Scientific) or 18-mm round glass coverslips (Marienfeld), depending on the experiments. 20 μg/ml laminin (Corning #354232) in Ca^{2+}/Mg^{2+}-free HBSS (Gibco) was used to coat the culture surface for at least 2 h before plating.

Live imaging and analysis of mitochondrial transport in cultured DRG neurons

DRGs were imaged at 3-4 days *in vitro* (DIV). Before imaging, cells were incubated with 200 nM of MitoTracker Deep Red for 30 min and the dye washed off prior to

imaging. Mitochondrial axonal transport was recorded with a Nikon spinning disk system comprising of a CSU-X1 scanning head (Yokogawa) and a Nikon Eclipse Ti-E inverted microscope equipped with a Du 897 iXon Ultra electron-multiplying charge coupled device camera (Andor) and a 60× CFI Apo/1.4 NA objective. Mitochondrial movements were typically recorded for 2 min with an acquisition rate of 0.5 frames/s, 640 nm excitation laser (5-10% power), 100-150 ms exposure, gain 1, EM gain 100. Temperature and CO_2 were maintained at 37°C and 5%, respectively, via a temperature unit with CO_2 control and a microscope enclosure (Okolab). Axonal transport was recorded approximately 100 μm away from the cell body and kymographs were produced by first straightening 100 μm of axonal tract (approximately in mid axon) using the Straighten plugin and followed by the Velocity Measurement Tool in ImageJ, as described previously [74,75]. Mitochondrial speed, run length and number of total mitochondria were analysed directly from the kymographs. Time-lapse movies were used to unambiguously confirm the mitochondrial tracks, when necessary. A mitochondrion was defined as motile if containing at least one continuous bout of net motion of at least 2 μm (a 'run') in the anterograde or retrograde direction. Because mitochondrial traces can be composed of multiple runs of variable speeds, velocity is defined as the average run velocities per single mitochondrion. Mitochondrial displacement is defined as the sum of the mitochondrial run lengths per single mitochondrion. Bidirectional mitochondria display at least one run in both the anterograde and retrograde directions.

Live imaging and analysis of mitochondrial transport in the mouse sciatic nerve

Exposure and *in vivo* imaging of intact sciatic nerve axons in anaesthetised mice were performed under terminal anaesthesia as previously described [76,77]. Time-lapse

imaging of mitochondrial transport was executed using an inverted LSM780 laser-scanning microscope (ZEISS) and 63× Plan-Apochromat oil immersion objective lens (ZEISS) at 100× digital zoom. Images were acquired at a rate of 0.5 frames/s for 8 min, with laser power 2%, resolution 1024×1024 and line averaging of 4. Analysis of mitochondrial motility was carried out essentially as described in [3]. Tracking of mitochondria was performed manually in Fiji/ImageJ on the raw movies using MTrackJ by marking the start and end of each run and tracking was performed blind to the age and sex of the animals. Speed and displacement were calculated from MTrackJ-generated tracks of runs ≥ 2 μm, as defined above. Total mitochondrial number was averaged from two frames at the beginning and at the end of the time series. The StackReg plugin of Fiji/ImageJ was used to correct for sample drifting, if necessary.

Live imaging of mitochondrial membrane potential and siRNA treatment

DRGs were cultured to DIV3-4 and incubated with 100 nM MitoTracker Green FM (Thermo Fischer Scientific) in DRG media for 30 min at 37°C. After washing off the dye, 50 nM TMRM (Thermo Fischer Scientific) was added to fresh media and incubated for 15 min. After washing off the TMRM dye with fresh media, imaging was performed with a Nikon A1RHD inverted confocal microscope, equipped with GaAsP and multi-alkali PMT detectors and a 60×/1.4NA Plan Apochromatic oil immersion objective. Cells were kept at a constant temperature of 37°C, 5% CO_2 throughout imaging. For both 488 nm (MitoTracker Green) and 561 nm (TMRM) excitation (laser power of 1% and 0.3%, respectively), we set the pixel dwell time at 2.2 μs, image size at 512×512, averaging at 2× and pinhole size at 39.6 μm. Low dye concentration and laser power were used to prevent TMRM quenching and FRET between dyes [17]. Quantification of fluorescent signal was performed using the raw intensity values in

Fiji/ImageJ. TMRM fluorescence intensity was measured and divided by the fluorescence signal of MitoTracker Green to obtain the normalised value of the mitochondrial membrane potential. For presentation purposes, the 'Smooth' filter in Fiji/ImageJ was used to reduce salt and pepper noise.

Dharmacon Accell SMARTpool Trak1 siRNA (Cat#E-056081-00-0010) and non-targeting control siRNA (Cat#D-001910-10-05) from Horizon Discovery were reconstituted to 100 μM following the manufacturer's instruction. When cultured DRGs reached DIV1, siRNAs were mixed with the Accell Delivery Media (ADM, Cat #B-005000-100) and, after removing 200 μl of conditioned media from each well of an 8-well imaging chamber, 200 μl of siRNA-ADM complexes were delivered dropwise on the cells at 1 μM final concentration (300 μl total media volume/well). After 72 h (DIV4), neurons were incubated with 4 μM of the JC-1 dye (Thermo Fisher Scientific) for 30 min and the media was replaced before imaging. The aggregation state of the dye is affected by $\Delta\Psi_m$ with the fluorescence emission shifting from green to red in more polarised mitochondria. The fluorescence emission at ~ 590 nm (red) and ~ 530 nm (green) was captured with emission filters ET595/50m and ET540/30m (both from Chroma Technology Corporation), respectively. The ~ 590/530 fluorescence ratio gives a measurement of $\Delta\Psi_m$. For trafficking studies, 0.5 μl non-targeting Green/6-FAM siRNA (Cat#D-001950-01-05) was added to the siRNA-ADM complexes to assess the efficiency of siRNA delivery.

Live cell calcium imaging

DRGs were imaged with a Nikon Ti-E inverted epifluorescence microscope equipped with a Nikon 20×/0.8 NA Plan Apochromat air objective, a mercury lamp (Nikon

Intensilight C-HGFI) for illumination and a Dual Andor Neo sCMOS camera for detection. Cells were plated on laminin-coated 18 mm coverslips and treated with 2 μm Rhod2-AM and 4 μm Fluo4-AM (both from Thermo Fisher Scientific) for 15 min at 37°C in external solution (145 mM NaCl, 2 mM KCl, 5 mM $NaHCO_3$, 1 mM $MgCl_2$, 2.5 mM $CaCl_2$, 10 mM glucose, 10 mM HEPES pH 7.4) [28] prior to imaging. Cells were imaged at DIV4 in a Ludin imaging chamber (Type 1, Life Imaging Services) in external solution at 1 frames/s for 3 min using GFP/mCherry filter set and exposure time of 30 ms. Cells were imaged for 30 s before transiently perfusing the imaging chamber with 50 mM KCl with a peristaltic pump (Ismatec). KCl was washed off after one minute and each coverslip was subjected to only one round of perfusion and imaging.

To quantify KCl-induced Fluo4 and Rhod2 response, a region of interest (ROI) was drawn to outline single cell bodies and axonal tracts from each field of view and the fluorescence intensity of the dyes measured in Fiji/ImageJ. Response curves were aligned at the base of the response peak and the fluorescence intensity at every time point was normalised to the value of the first frame. Fluorescence 'peak' was defined as the maximum fold-change value reached during imaging and the time to reach the peak was calculated as the Δt between the 'peak' timepoint and the time of first response to stimulation, as reported previously [74].

GEMs viral preparation and transduction

To obtain GEMs-encoding lentiviral particles, the pCMV-PfV-Sapphire-IRES-tdTomato plasmid (Addgene, #116934) [36] was transfected into Lenti-X 293T cells (TaKaRa, #632180) using the polyethylenimine(PEI)-based Transporter 5 transfection reagent (Polysciences, #26008) and a 2nd generation viral packaging system

comprising gag/pol/tat/rev (psPAX2, Addgene, #12260) and VSV-G (pMD2.G, Addgene, #12259). Cells were seeded in a 15 cm dish in 22.5 ml media (DMEM with 4.5g/l glucose and pyruvate, 10% hi-FBS, 1x GlutaMAX) at 37°C with 5% CO_2 until they reached 60-80% confluency. The media was then replaced and cells incubated for 2 h with fresh media containing 2% FBS. DNA-PEI complexes (14.6 μg psPAX2, 7.9 μg pMD2.G, 22.5 μg GEM-transfer vector and 135 μl Transporter 5) were prepared according to the manufacturer's instructions and added dropwise to the cells. After overnight incubation, the medium was replaced with 17 ml fresh media with 2% FBS, the supernatant harvested 3 times every 8-12 h and kept at 4°C. Typically, the three harvests were centrifuged at 500 *g* for 5 min at 4°C before filtering through 0.22 µm filter units and further ultracentrifugation at 50,000 x *g* for 2 h at 4°C. After gently discarding the supernatant, the viral pellet was let dry for 2-3 min before resuspension in DMEM without FBS or Opti-MEM to obtain a 1000-fold concentration and stored at -80°C in 10-20 μl aliquots. Between 1-10 μl of concentrated virus was added to each well of a μ-Slide 8-well glass bottom imaging chambers.

GEMs imaging and single particle analysis

DRGs were plated in μ-Slide 8-well glass bottom imaging chambers and the concentrated lentiviral particles added at DIV4. The media was replaced after 24 h with fresh media without growth factors and the cells imaged after an additional 36 h (DIV7) by spinning disk confocal microscopy with a Nikon 100×/NA 1.40 CFI Plan Apo VC objective and 100 ms continuous acquisition for 30 s, 488 nm laser at 40-50% intensity, gain 1, EM gain 250. Cells expressing similar levels of transduced construct, as assed by the tdTomato signal, were selected for imaging.

Single particle tracking (SPT) was performed on raw time series using TrackMate on selected ROIs defining the cell body and axonal compartments using the DoG detector for small spot detection (<5 pixels), with estimated particle diameter set at 0.4-0.5, thresholds between 0.4-0.6. with median filter and sub-pixel localization. The Simple LAP tracker was used to link the particles throughout the movie (linking max distance = 1, gap-closing max distance = 1.6, gap-closing max frame gap = 2). Tracks were then exported and analysed in MATLAB. Time-averaged mean square displacement (MSD) was calculated via creation of a SPT Analyser using a custom script (available on request). The mean diffusion coefficient (D_{eff}) was calculated by fitting the first 10 s of the time-averaged MSD with the equation $MSD\ (t) = 4Dt^{\alpha}$, where α is the exponent describing the anomalous diffusion and D is the diffusion coefficient.

FLIM

Calibration and FLIM measurements were carried out essentially as in Steinmark et al. [20]. DRGs were plated in μ-Slide 8-well glass bottom imaging chambers. On the day of imaging (DIV3-4), cells were washed in external solution and incubated with 1 μM FMR-1 for 30 min at 37°C and the dye was washed off prior to imaging. Cells were imaged on an inverted TCS-SP2 microscope (Leica Microsystems) using two SPC-150 TCSPC boards (Becker & Hickl). FMR-1 was excited using a picosecond-pulsed (90 ps optical pulse width, 20 MHz repetition rate) 467 nm diode laser (Hamamatsu, Japan) using a HCX PL APO CS 63X 1.2 NA water objective, with a 485 nm dichroic mirror and a 514/30 nm band pass filter. All measurements were carried out at 37°C and 5% CO_2. Analyses were performed at single cell level by measuring the fluorescence lifetime separately in cell bodies and proximal-mid axons regions.

TR-FAIM

DRG neurons were grown to DIV3-4, as for the FLIM experiments, and labelled with 1 μM BCECF (Themo Fisher Scientific #B1150) for 30 min at 37°C. The dye was washed off prior to imaging in FluoroBrite DMEM. Time-resolved anisotropy measurements were conducted on the same TCS-SP2 microscope system used for FLIM, with the BCECF dye excited using a picosecond-pulsed laser. In this case, the fluorescence emission was split into its parallel and perpendicular components using a polarizing beam splitter (Edmund Optics).

Calibration curve. Rotational correlation times of BCECF in solutions of increasing viscosity (through addition of glycerol) were measured and plotted. To avoid depolarisation effects from the objective, a 5x NA 0.15 objective was used and measurements were conducted at room temperature, but otherwise the setup was identical to that described above. The anisotropy was calculated using the equation:

$$r(t) = \frac{I(t)_{par} - GI(t)_{perp}}{I(t)_{par} + zGI(t)_{perp}} \quad (1)$$

Where z = 2 and G is a correction factor used to correct for the different sensitivity of the two detectors. It is calculated by taking the tail value of:

$$G = I(t)_{par}/I(t)_{perp} \quad (2)$$

G-values used were around 1 +/- 0.1. Here the G-factor was measured using a solution of fluorescein in water and 10% glycerol. The calibration curve was calculated to avoid assumptions about molecular shape and diffusion boundary conditions in a classic Stokes-Einstein-Debye calculation.

Fluorescence Anisotropy decay. For each raw neuron image, two regions of interests (ROIs) were extracted: from the axon and the soma. For each ROI, a single set of

parallel and perpendicular decays were generated by summing the photon counts in each time bin over all pixels within the given ROI. Anisotropy pre-processing, curve fitting and graphing were performed in OriginLab. The perpendicular (I_{perp}) and parallel (I_{par}) decays for each ROI of each image were aligned and the anisotropy decay was calculated using equation (1) where z, due to the high NA of the objective, was determined to be 1, and G was determined as described above. Analyses were performed at single cell level by calculating anisotropy separately on cell bodies and proximal-mid axon region of the same cell. For calculating the anisotropy of an entire cell, the soma and axon photon counts were summed up and analysis was performed as described. It was established that the hindered rotation model (below) provides an optimum fit for most anisotropy decays, accounting for a restricted model of rotation in all environments.

$$r_{model} = (r_0 - r_\infty)e^{\frac{-t}{\theta}} + r_\infty \quad (3)$$

Where r_0 is the initial anisotropy, r_∞ is the limiting anisotropy and Θ is the rotational correlation time. The weighting factor v(r) for the anisotropy fits was the variance of r [78]:

$$v(r) = \frac{(1-r)(1+2r)(1-r+G(1+2r))}{3G} \quad (4)$$

Only the first 10 ns of the decay were used for the fit and only meaningful fits with an acceptable adjusted R-squared value and standard errors of the parameter fits were accepted for further analysis.

Statistical analyses.

Details of the statistical analyses are reported in the figure legends. Shapiro-Wilk test was performed to test data for normal distribution before determining the appropriate

statistical test. Sample sizes, which were predetermined using power calculations and previous experience, are also reported in figure legends.

FIGURES

Figure 1

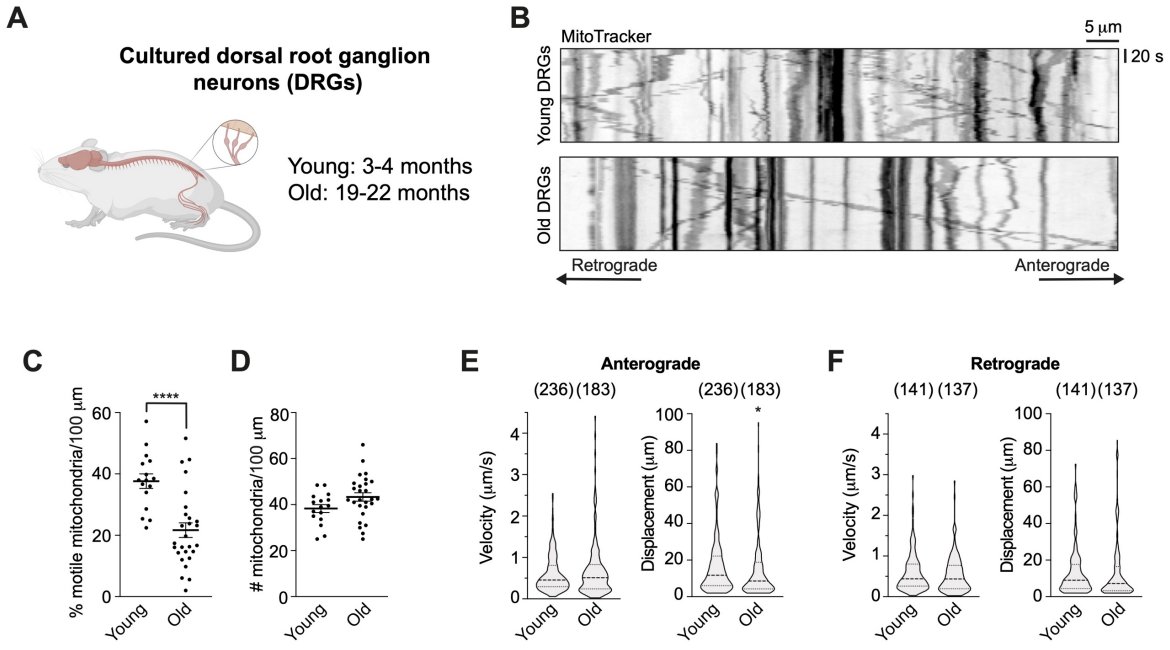

Figure 1. Mitochondrial transport is reduced in aged DRG neurons in culture

(A) DRGs were dissected from the spinal cord of 6 young (P72-107, 3 females and 3 males) and 6 old (P560-637, 3 females and 3 males) mice and dissociated neurons were cultured *in vitro.* **(B)** Representative kymographs of mitochondria moving in the axons of DRG neurons dissected from young and old animals. **(C-D)** The proportion of motile mitochondria (C), but not the mitochondrial mass (D), is strongly reduced during ageing in the DRG neuron axons. Individual data points represent fields of view (FOV) imaged (1-3 axons/FOV). **(E-F)** Anterograde and retrograde mitochondrial velocity (E) and displacement (F) remain largely stable during ageing, albeit with a subtle but significant reduction in anterograde displacement in aged neurons. In brackets, number of mitochondria. Data are shown as mean ± SEM. Unpaired student's t-test (C-D), Mann-Whitney test (E-F). * $p < 0.05$; **** $p < 0.0001$.

Figure 2

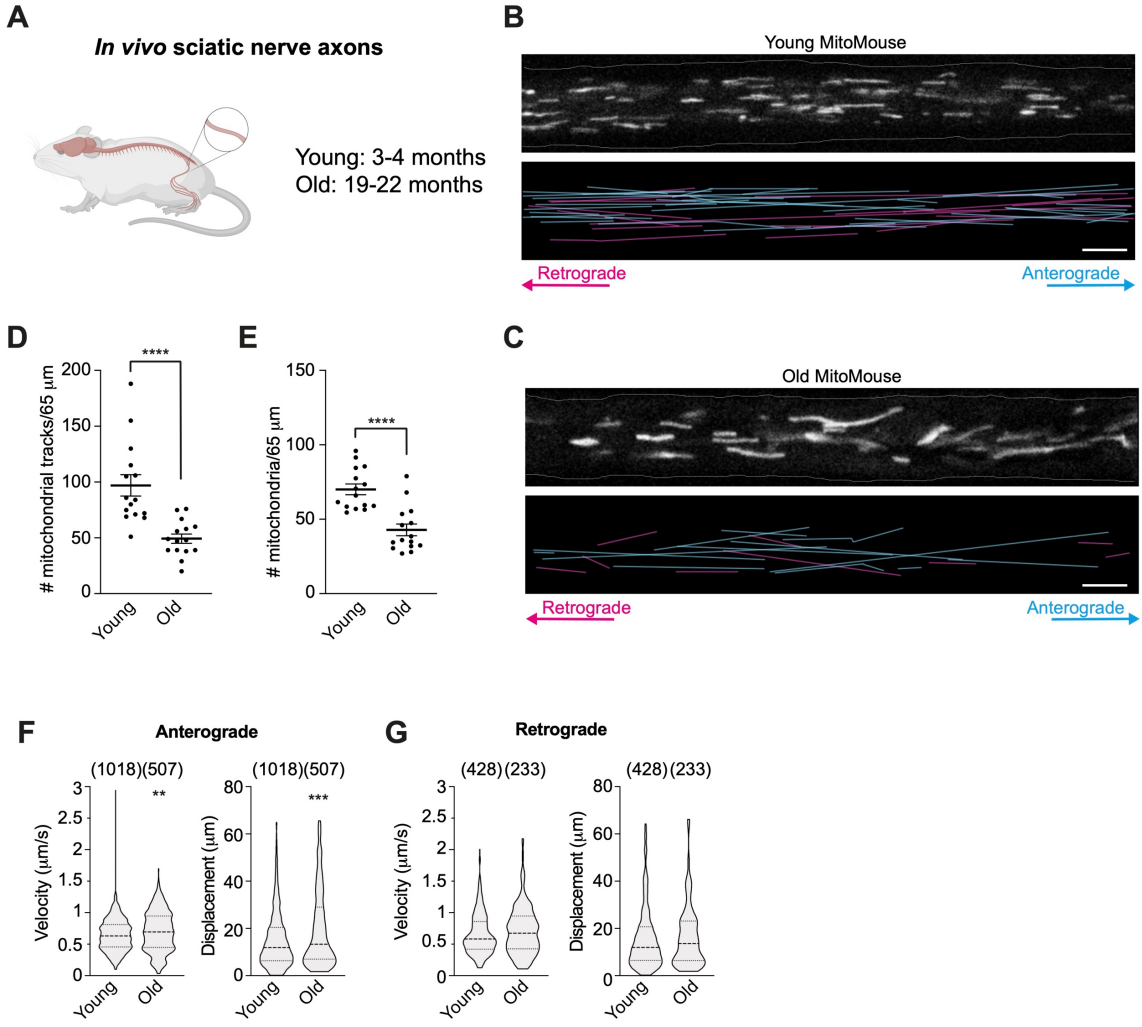

Figure 2. Mitochondrial transport decreases with age in the sciatic nerve *in vivo*

(A) 5 young (P72-107, 3 females and 2 males) and 5 old (P560-637, 2 females and 3 males) MitoMice were anesthetised and the sciatic nerve exposed for time-lapse imaging of mitochondrial axonal transport. **(B-C)** Still frames from movies showing mitochondria (grey, top panels) in single sciatic nerve axons from young (B) and old (C) MitoMice. The bottom panels depict the traces of mitochondria moving in the anterograde and retrograde directions (cyan and magenta, respectively) in the corresponding movies. Scale bars: 5 µm. **(D-E)** Both the number of motile mitochondria and the total number of mitochondria present in the axons of the sciatic

nerve are strongly reduced during ageing. Individual data points represent individual sciatic nerve axons. **(F-G)** Mitochondrial anterograde velocity and displacement are both upregulated in old neurons (F), while the motile properties of the retrograde-moving mitochondria are not affected by age (G). In brackets, number of mitochondria. Data are shown as mean ± SEM. Mann-Whitney test (D-G). ** $p < 0.01$; *** $p < 0.001$; **** $p < 0.0001$.

Figure 3

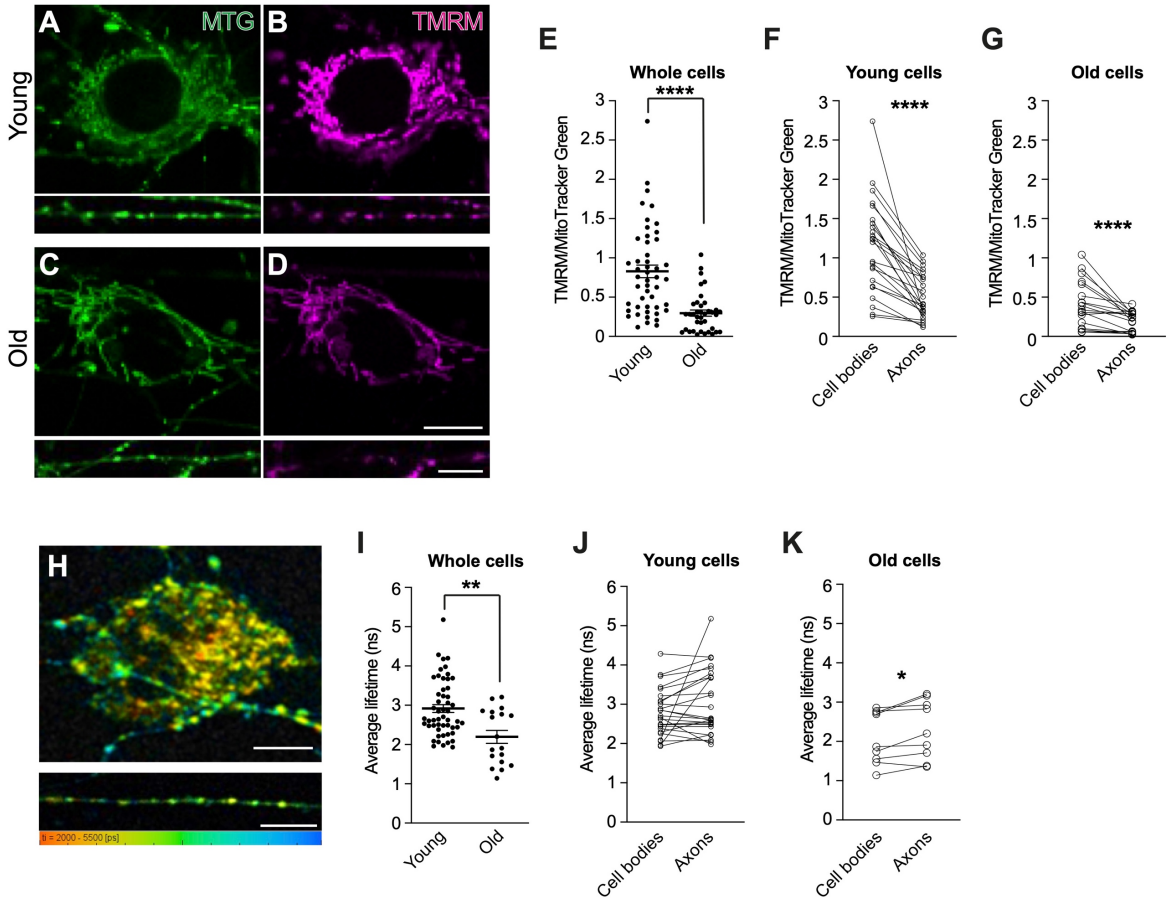

Figure 3. Mitochondrial membrane potential and viscosity decline during ageing **(A-D)** Representative images of young (A-B) and aged (C-D) DRG neuron cell bodies (top panels) and axons (bottom panels), stained with TMRM and MitoTracker Green (MTG). Scale bars: 10 µm. **(E-G)** Quantification of the ratio between TMRM and MTG in neuronal cell bodies and axons combined indicates that the $\Delta\Psi_m$ declines during ageing at cellular level (E) with axonal mitochondria displaying consistently reduced $\Delta\Psi_m$ in both young (F) and old (G) cells. **(H)** Representative images of a DRG neuron cell body (top panel) and axon (bottom panel) stained with FMR-1 to capture mitochondrial viscosity. Rainbow colour scale indicates fluorescence lifetime range (2,000-5,500 ps) in which orange/red and cyan/blue hues correspond to areas of lower

and higher viscosity, respectively. Scale bars: 15 μm. **(I)** Overall mitochondrial viscosity is decreased in old cells, as indicated by quantification in neuronal cell bodies and axons combined. **(J-K)** There is no significant difference between somal and axonal mitochondrial viscosity in young DRG neurons (J), while mitochondrial viscosity is slightly higher in old DRG axons (K). In E-G and I-K, data points represent the cell bodies and axons imaged. Each neuron analysed provides both cell body and axons to the analysis. DRGs were dissected from 3 young (P49-67, 1 female and 2 males) and 3 old (P672-679, 2 females and 1 male) mice for TMRM experiments (A-G), and from 3 young (P81-84, 2 females and 1 male) and 2 old (P715, 1 female and 1 male) mice for FLIM experiments (H-K). Data are shown as mean ± SEM. Mann-Whitney test (E, I), paired student's t-test (F, K), Wilcoxon test (G, J). * $p < 0.05$; ** $p < 0.01$; **** $p < 0.0001$.

Figure 4

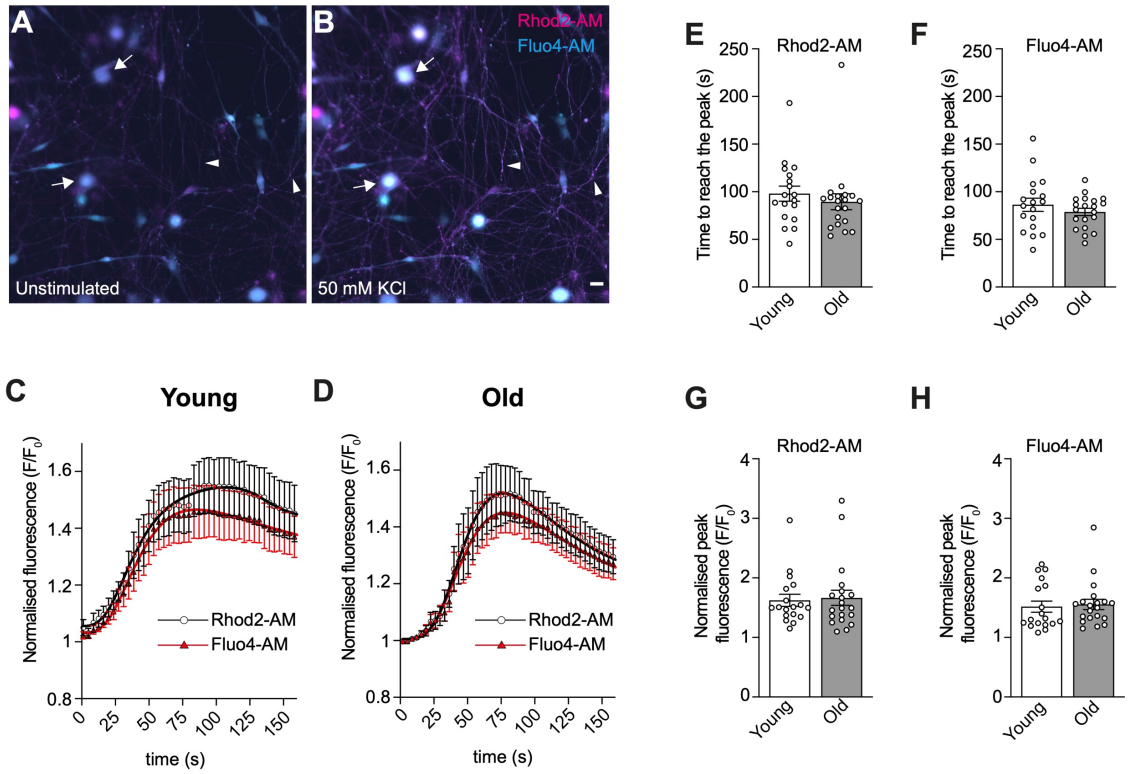

Figure 4. Mitochondrial and cytosolic calcium uptake are not significantly affected by age in cultured DRG neurons

(A-B) Representative images of DRGs cultured before (A) and after (B) stimulation with 50 mM KCl. Cells are co-stained with Rhod2-AM (magenta) and Fluo4-AM (cyan) for measuring the fluorescent signal of mitochondrial and cytosolic Ca^{2+}, respectively. Neuronal depolarisation by KCl increases calcium uptake in cell bodies (arrows) and axons (arrowheads). Scale bar: 20 μm. **(C-D)** Traces indicate the average Rhod2-AM (black, circles) and Fluo4-AM (red, triangles) fluorescence intensity values in 18 young (C) and 20 old (D) neurons at individual time points (circles and triangles, respectively) normalised to the average fluorescence value before KCl stimulation (time 0). **(E-F)** Time to reach the peak and **(G-H)** normalised response peak for cytoplasmic (Fluo4-AM) and mitochondrial (Rhod2-AM) calcium. Mann-Whitney tests (E,G-H) and an unpaired student's t-test with Welch's correction (F) showed no difference between

conditions. DRGs were obtained from 3 young (P58-93, 3 males) and 4 old (P560-676, 1 female, 3 males) mice.

Figure 5

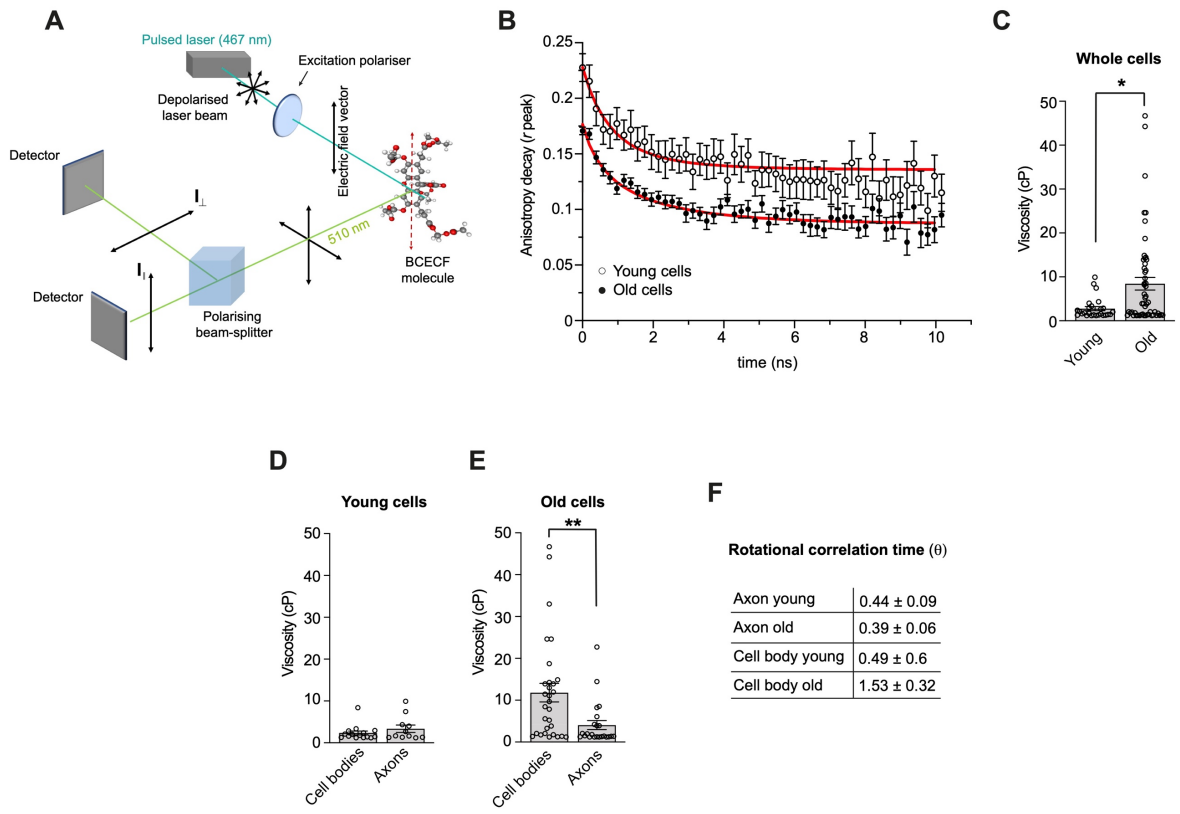

Axon young	0.44 ± 0.09
Axon old	0.39 ± 0.06
Cell body young	0.49 ± 0.6
Cell body old	1.53 ± 0.32

Figure 5. The cytoplasmic viscosity of aged DRG neurons in culture increases in cell bodies but not in axons

(A) Schematic of the fluorescence anisotropy optical set up. A 467 nm depolarised pulsed laser beam (cyan) is linearly polarised before exciting BCECF molecules with a transition dipole (dashed red line) parallel to the electric field vector of the light. The 510 nm emitted light (green) is passed into a polarising beam splitter to two detectors for light with either parallel ($I_{\parallel}$) or perpendicular ($I_{\perp}$) emission polarisation. The rotational correlation time (θ) of the BCECF molecule is defined as the time taken to rotate one radian (during the fluorescence lifetime). **(B)** Fluorescence anisotropy decay and fit (see Methods, equation 3) of BCECF fluorescence obtained from perpendicular and parallel decays (according to equation 1, see Methods) from young and old DRG neurons. Older cells display a slower decay, indicative of higher

cytoplasmic viscosity. Red lines show the exponential decay fit and circles the individual time points. **(C)** Viscosity values obtained from anisotropy decay analysis show increased viscosity in old DRG neurons. Circles show individual cellular compartments. Relative to (B). **(D-E)** The somal and axonal compartments display similar viscosity values in young DRG neurons (D, $p = 0.5065$), whereas the cytoplasmic viscosity of old DRG neurons is significantly higher in the somal compartment. Circles depict individual cellular compartments. **(F)** Rotational correlation time (θ) values relative to somal and axonal anisotropy data. Note the average θ is proportional to viscosity. Data are shown as mean ± SEM, Mann-Whitney test. * $p < 0.05$; ** $p < 0.01$. DRGs for the anisotropy experiments were obtained from 2 young (P80) and 3 old (P709-712) male mice.

Figure 6

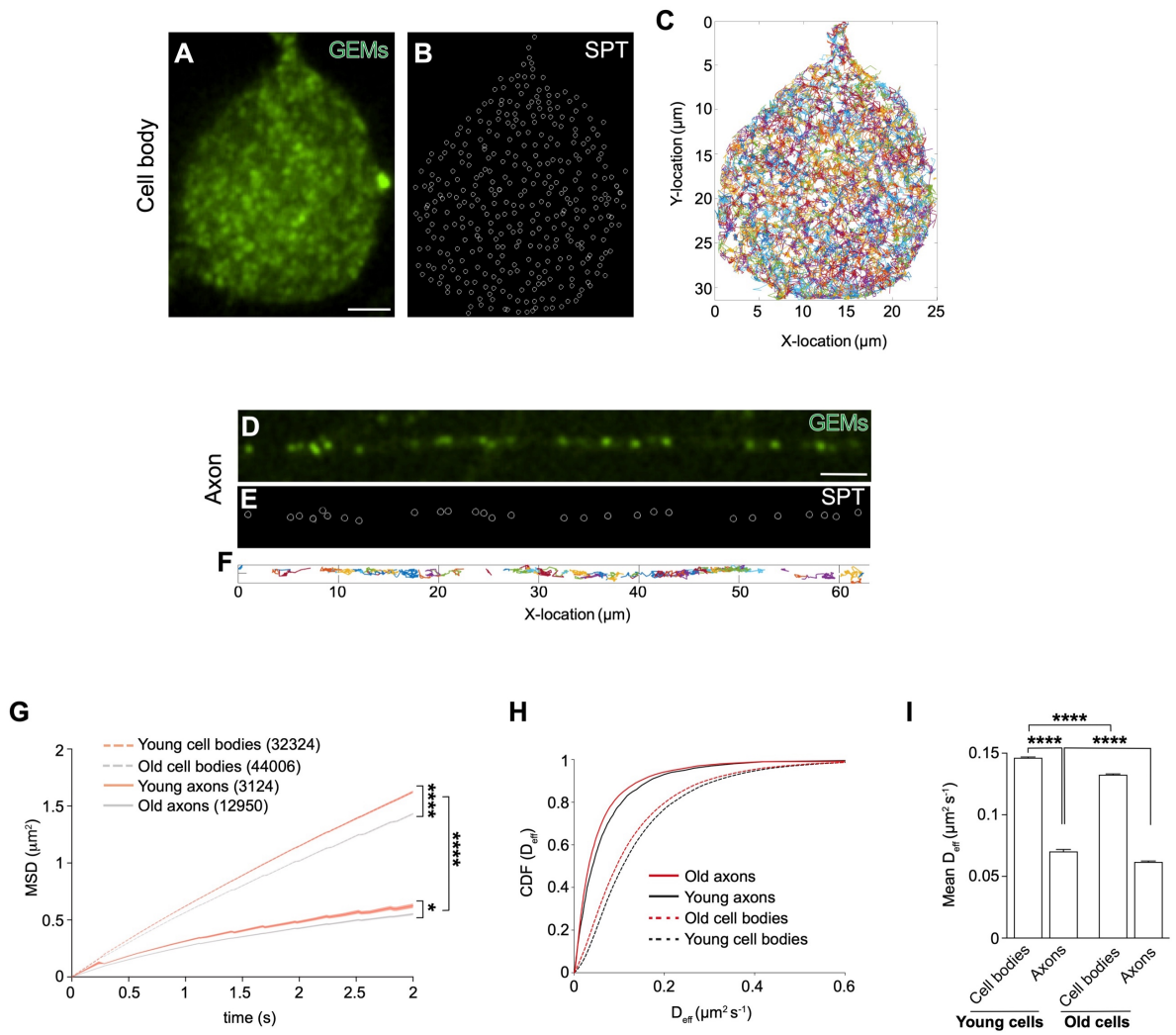

Figure 6. The diffusiveness of the neuronal cytoplasm decreases in aged cultured neurons

(A-F) Representative images of a cell body (A-C) and axon (D-F) of a DRG neuron transduced with lentiviral vectors expressing GEMs. In (B) and (E), single particle tracking (SPT) markers are overlayed onto the cell body and axons, respectively. (C) and (F) show the colour-coded GEMs trajectories tracked during 30 s of imaging of (B) and (E), respectively. Scale bars: 5 µm. **(G)** Mean square displacement (MSD) of GEM tracks in cell bodies and axons of young and old cells. Data are plotted as mean ± SEM, Kolmogorov-Smirnov test. The motion of GEMs is captured by a sub-diffusion

model described by the equation $MSD\ (t) = 4Dt^{\alpha}$ (young cell bodies: R = 0.999, old cell bodies: R = 1, young axons: R = 0.997, old axons: R = 1). In brackets, number of tracks analysed from 61 cell bodies and 170 axons. **(H)** Cumulative distribution function (CDF) of GEMs diffusion coefficient (D_{eff}) in young and old DRG axons (black and red lines, respectively) and young and old cell bodies (black and red dashed lines, respectively). Relative to (G). **(I)** Mean diffusion coefficient in the cell body and axonal compartments of young and old cells. Relative to (H). DRGs for the microrheology experiments were obtained from 2 young (P49-70) male mice and 2 old (P726-757, 1 female and 1 male) mice. Data are presented as mean ± SEM, Kruskal-Wallis with Dunn's multiple comparisons test. * $p < 0.05$; **** $p < 0.0001$.

Figure 7

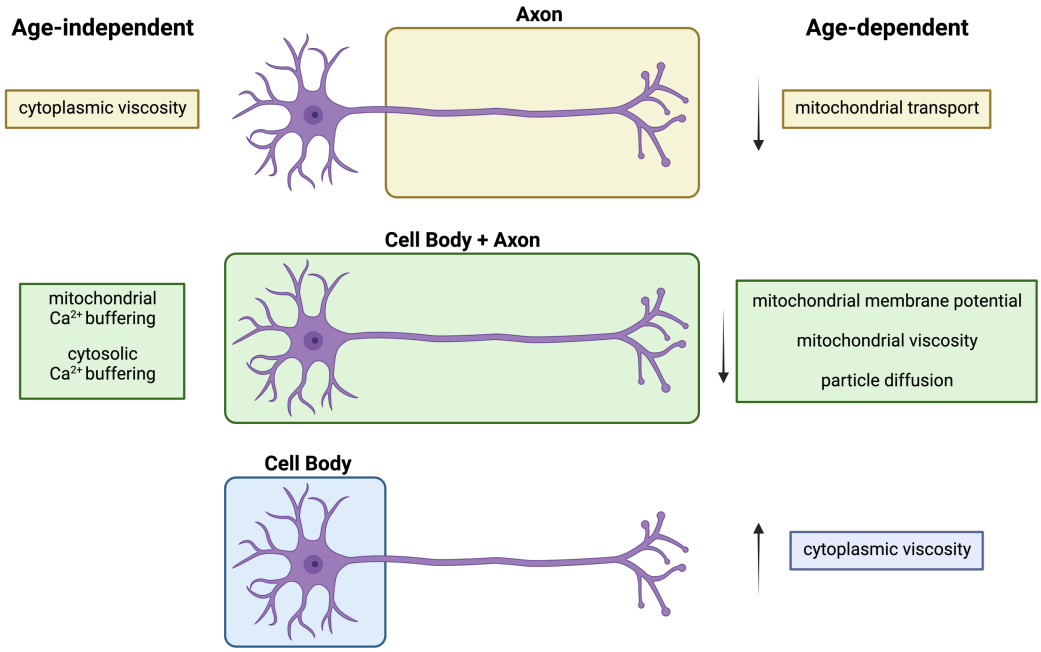

Figure 7. Model of mitochondrial homeostasis and cytoplasmic viscosity during ageing

Decreased axonal mitochondrial transport characterises the ageing process of mouse DRG neurons *in vivo* and *in vitro* ('Age-dependent', yellow). The overall decrease in mitochondrial membrane potential observed in aged DRG cultured neurons correlates with reduced intra-mitochondrial viscosity both in the cell bodies and axons ('Age-dependent', green) but not with their capacity to buffer calcium, which is unaffected in aged cultures ('Age-independent', green). Cytoplasmic viscosity is upregulated in the cell bodies ('Age-dependent', blue), but not in axons ('Age-independent', yellow). Compartment-dependent and age-specific changes may reflect functional specialisation of the mitochondria and specific regulation of viscosity across sub-cellular compartments and time.

Supplementary Figure 1

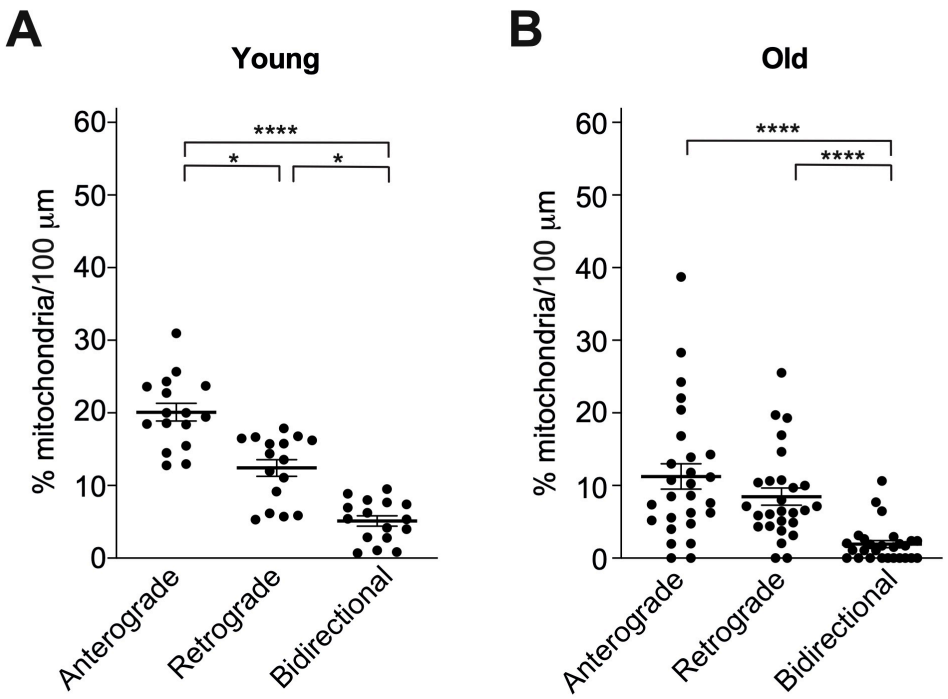

Fig. S1

Proportion of motile mitochondria displaying anterograde, retrograde and bidirectional motility in young **(A)** and old **(B)** neurons (relative to Figure 1C). A general decrease of motility is observed during age. Individual data points represent fields of view (FOV) imaged (1-3 axons/FOV). Data are shown as mean ± SEM. Kruskal-Wallis with Dunn's multiple comparisons test. * $p < 0.05$; **** $p < 0.0001$.

Supplementary Figure 2

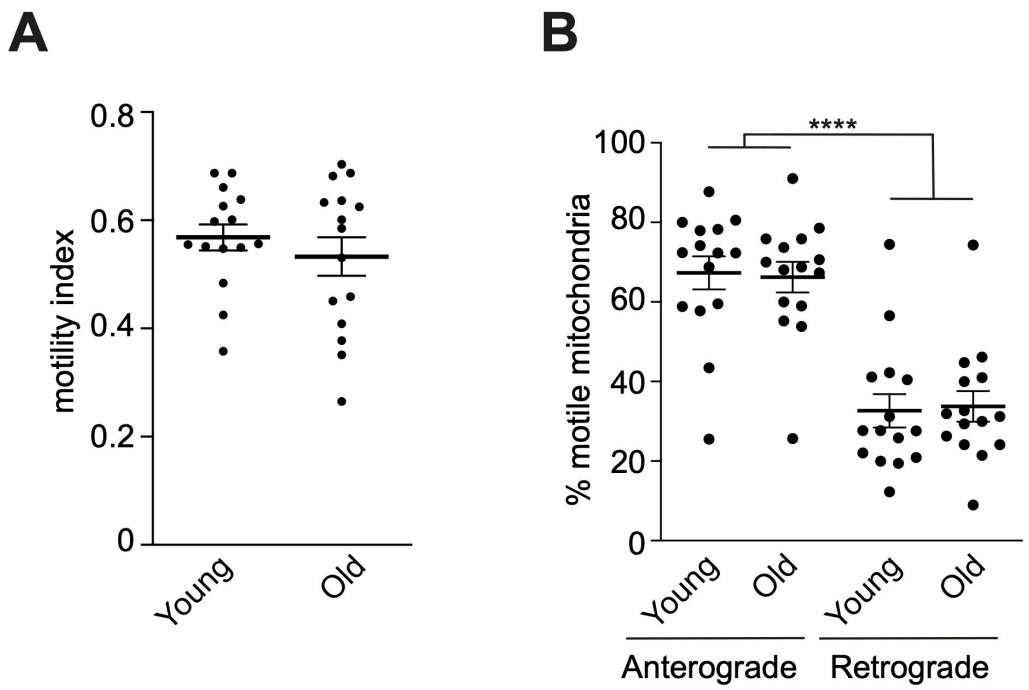

Fig. S2

(A) There is no difference in the mitochondrial motility index between young and old neurons (*i.e.*, total moving mitochondria/(total moving + stationary mitochondria)). **(B)** The relative proportions of anterograde and retrograde mitochondrial transport are not changed by age in the sciatic nerve, indicating that the reduction of both types of transport contributes to the overall transport decline (Figure 2D). Individual data points represent fields of view (FOV) imaged (1-3 axons/FOV). Data are shown as mean ± SEM. Unpaired student's t-test (A), two-way ANOVA with Tukey's multiple comparisons test (B). **** $p < 0.0001$.

Supplementary Figure 3

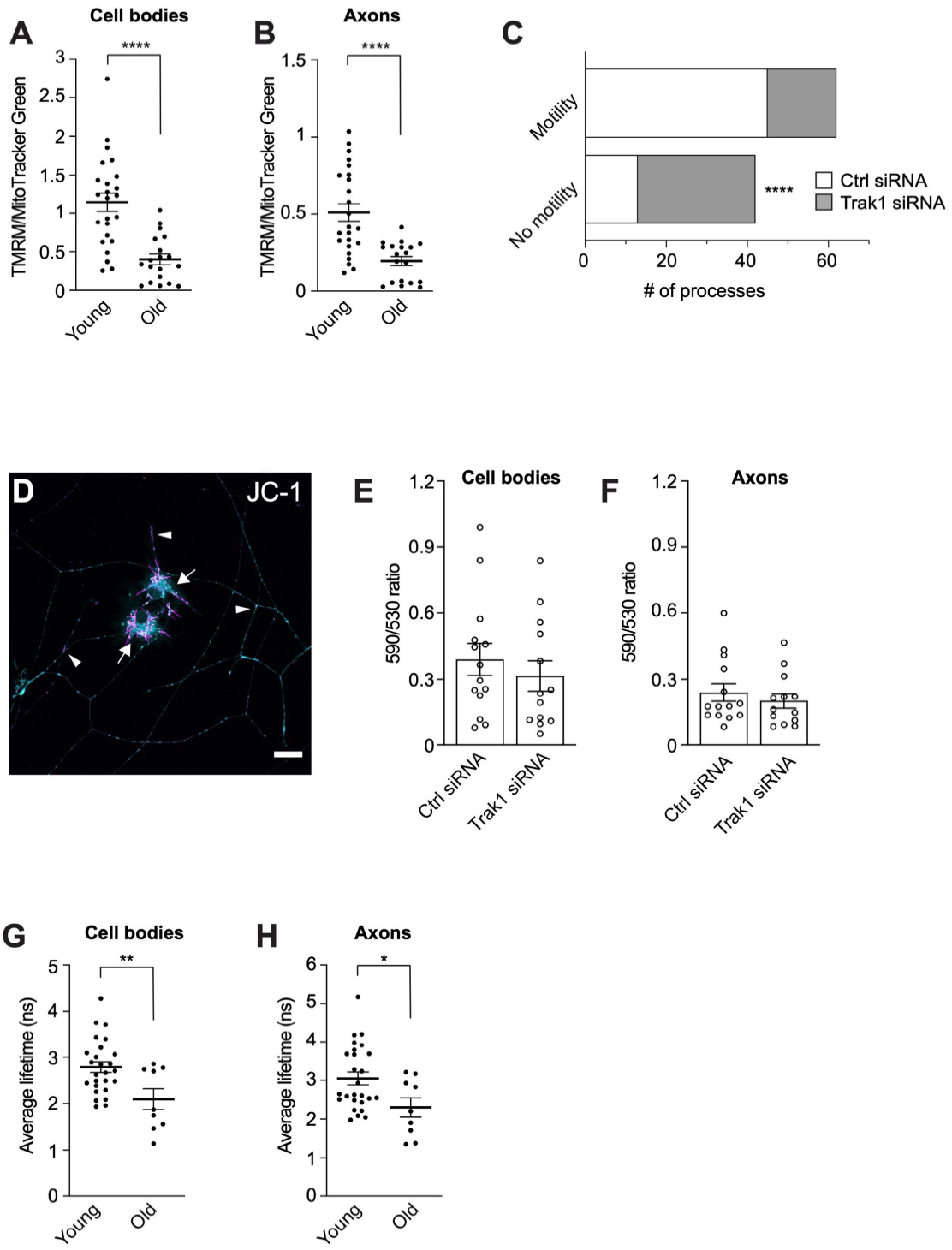

Fig. S3

(A-B) Quantification of the ratio between TMRM and MTG in neuronal cell bodies (A) and axons (B) indicates that the $\Delta\Psi_m$ declines during ageing in both compartments.

(C) Increased number of DRG neuron axons displaying no motile mitochondria after Trak1 RNAi. A process is scored as displaying motility if at least two mitochondria are motile within one minute of imaging. Number of axons analysed are 58 (Ctrl siRNA) and 46 (Trak1 siRNA). **(D)** DRG neurons stained with the JC-1 vital dye and pseudocoloured in cyan and magenta (~ 530 and ~ 590 nm emission, respectively). Arrows, somal compartments; arrowheads, axons. Note the higher polarisation of somal mitochondria compared to axonal mitochondria, indicated by widespread magenta, corroborating the data in Fig. 3A-G. Scale bar: 20 μm. **(E-F)** Trak1 RNAi does not significantly change the ~ 590/530 JC-1 ratio in the cell bodies (E) or axons (F) of DRG neurons, suggesting the $\Delta\Psi_m$ is not affected by this manipulation. Data points represent individual cell bodies and axons, respectively. Each neuron analysed provides both cell body and axons to the analysis. DRGs for JC-1 quantifications were obtained from 3 young (P102-105) male mice. **(G-H)** Mitochondrial viscosity decreases during age both in the cell bodies (G) and axons (H) of DRG neurons. Data points represent cell bodies and axons imaged. Data are shown as mean ± SEM. Unpaired student's t-test (A, E, G), Mann-Whitney test (B, F, H), Fisher's exact test (C). * $p < 0.05$; ** $p < 0.01$; **** $p < 0.0001$.

Supplementary Figure 4

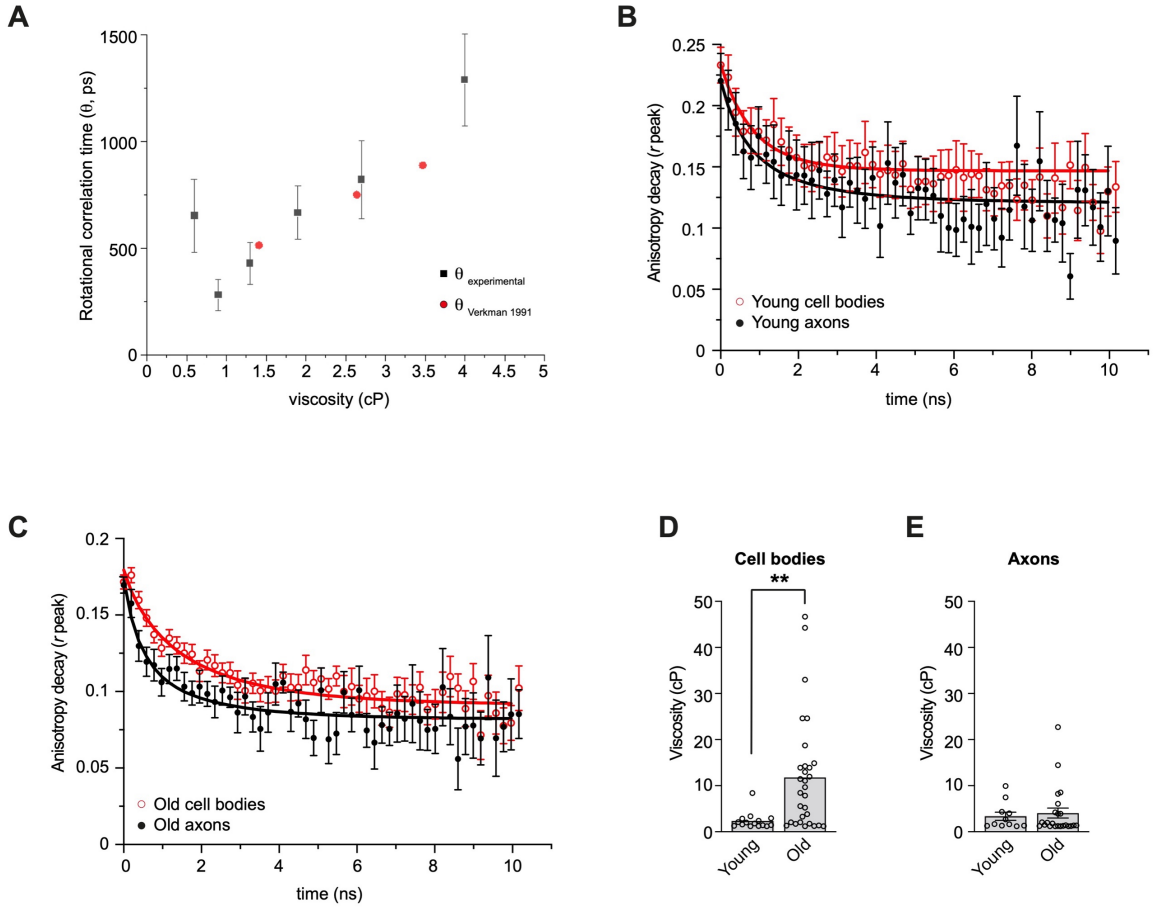

Fig. S4

(A) Calibration curve of BCECF rotational correlation time (θ) calculated in accordance with the Stokes-Einstein-Debye equation. The experimental data were compared to historical data for BCECF θ as a function of viscosity [79] and showed good agreement. **(B-C)** Fluorescence anisotropy decay and fit (see Methods, equation 3) of BCECF fluorescence obtained from perpendicular and parallel decays (according to equation 1, see Methods) from cell bodies and axons of young (B) and old (C) DRG neurons. Red and black lines depict exponential decay fit for cell bodies and axons, respectively. The anisotropy decay of young cells (B) is not significantly different between compartments, leading to similar viscosity values (Fig. 5D). The slower decay

of cell bodies compared to axons in old DRGs is indicative of higher viscosity, as shown in Fig. 5E. Circles, individual time points. **(D-E)** Cytoplasmic viscosity increases during age in the cell bodies (D) but not axons (E) of DRG neurons. Circles depict cell bodies and axons imaged. Data are shown as mean ± SEM. Mann-Whitney test (D-E). ** $p < 0.01$.

Supplementary Figure 5

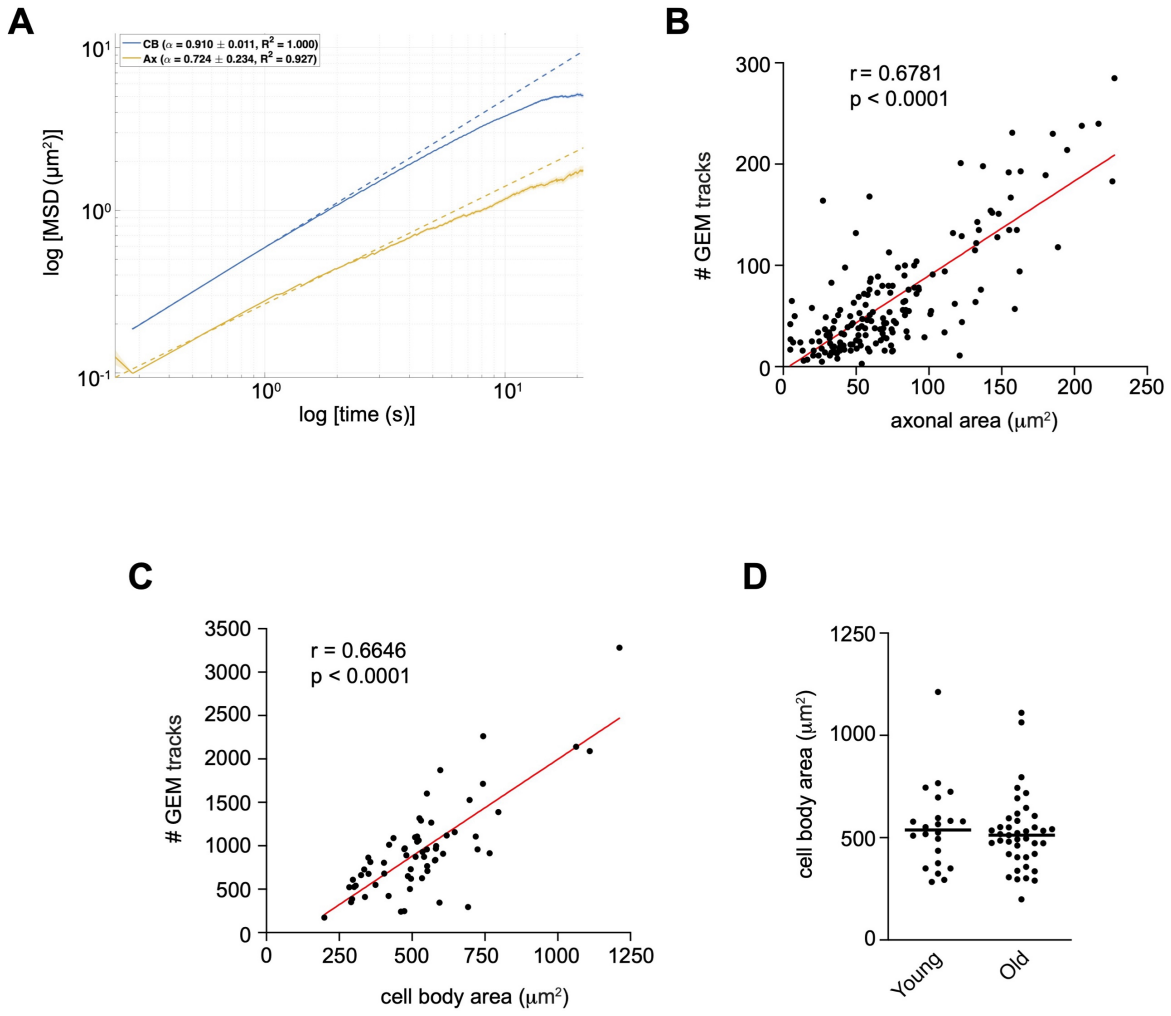

Fig. S5

(A) Combined MSD of GEM tracks in cell bodies (CB, blues) and axons (Ax, orange). Data are plotted as mean ± SEM in a log-log format. Dashed lines are curve fit with anomalous exponent of 0.910 ± 0.011 (CB) and 0.724 ± 0.234 (Ax), respectively. **(B-C)** Highly positive correlation between total number of GEMs tracks analysed and axonal (B) and cell body (C) areas, suggesting that GEMs equally cover the full extent of the neuronal cytoplasm, independently of cell size. Circles represent individual axons (B) and cell bodies (C). Red lines, linear regression fit. Spearman rho test. **(D)**

There is no significant difference between the mean area of the young and old cell bodies, indicating that cell size is unlikely to affect viscosity and diffusiveness. Circles represent individual cell bodies. Data are shown as mean ± SEM. Mann-Whitney test ($p = 0.5148$).

Supplementary Table 1

A. Young

Velocity (μm/s)			
Anterograde		Retrograde	
In vivo	*In vitro*	*In vivo*	*In vitro*
0.63 (2.55), n = 1018	0.45 (2.94), n = 236 ****	0.58 (2.01), n = 428	0.44 (2.98), n = 141 ****
Displacement (μm)			
Anterograde		Retrograde	
In vivo	*In vitro*	*In vivo*	*In vitro*
11.86 (64.92), n = 1018	11.73 (83.80), n = 236	11.95 (64.26), n = 428	9.02 (72.47), n = 141 **

B. Old

Velocity (μm/s)			
Anterograde		Retrograde	
In vivo	*In vitro*	*In vivo*	*In vitro*
0.69 (1.7), n = 507	0.51 (4.41), n = 183 ****	0.67 (2.17), n = 233	0.43 (2.85), n = 137 ****
Displacement (μm)			
Anterograde		Retrograde	
In vivo	*In vitro*	*In vivo*	*In vitro*
13.31 (65), n = 507	8.62 (95.13), n = 183 ****	13.58 (65), n = 233	7.21 (85.50), n = 137 ****

Table S1

Median mitochondrial velocities and displacements are significantly higher in the sciatic nerve axons (*in vivo*) compared to DRG axons (*in vitro*) in all conditions except for anterograde displacement in young samples (A) where no difference was detected. Values are medians with, in brackets, maximum speeds and maximum displacements. n = number of mitochondria, Mann-Whitney test. ** $p < 0.01$; **** $p < 0.0001$. The data suggest that, while mitochondria are able to reach faster maximum velocities *in vitro*, on average they move more slowly *in vitro* than *in vivo*. Note that the displacement is calculated over 65 μm and 100 μm of axonal tract in the sciatic nerve and cultured DRGs, respectively, suggesting the calculated values may underestimate the significance between *in vivo* and *in vitro* displacements.

Movie 1

Representative time-lapse movie of mitochondria from young (P72) and old (P624) MitoMouse sciatic nerve axons. Width: 64 µm. Movie plays at 20 frames per seconds and represents 4:26 minutes of real-time. The 'Smooth' filter in Fiji/ImageJ was applied for presentation purposes.

Movie 2

Representative time-lapse movie of GEM particles in the cell body of a cultured DRG neuron. Movie plays at 20 frames per seconds and represents 30 seconds of real-time.

Movie 3

Representative time-lapse movie of GEM particles in the axon of a cultured DRG neuron. Width: 55 µm. Movie plays at 20 frames per seconds and represents 30 seconds of real-time. The 'Smooth' filter in Fiji/ImageJ was applied for presentation purposes.

Bibliography.

1. López-Otín, C., Blasco, M. A., Partridge, L., Serrano, M. & Kroemer, G. Hallmarks of aging: An expanding universe. *Cell* **186**, 243–278 (2023).
2. Vagnoni, A., Hoffmann, P. C. & Bullock, S. L. Reducing Lissencephaly-1 levels augments mitochondrial transport and has a protective effect in adult Drosophila neurons. *J. Cell Sci.* **129**, 178–90 (2016).
3. Vagnoni, A. & Bullock, S. L. A cAMP/PKA/Kinesin-1 Axis Promotes the Axonal Transport of Mitochondria in Aging Drosophila Neurons. *Curr. Biol.* **28**, 1265–1272 (2018).
4. Morsci, N. S., Hall, D. H., Driscoll, M. & Sheng, Z.-H. Age-Related Phasic Patterns of Mitochondrial Maintenance in Adult Caenorhabditis elegans Neurons. *J Neurosci* **36**, 1373–1385 (2016).
5. Takihara, Y. *et al.* In vivo imaging of axonal transport of mitochondria in the diseased and aged mammalian CNS. *Proc. Natl. Acad. Sci. U. S. A.* **112**, 10515–10520 (2015).
6. Mattedi, F. & Vagnoni, A. Temporal Control of Axonal Transport: The Extreme Case of Organismal Ageing. *Front. Cell. Neurosci.* **13**, 393 (2019).
7. Elbaum-Garfinkle, S. & Brangwynne, C. P. Liquids, Fibers, and Gels: The Many Phases of Neurodegeneration. *Dev. Cell* **35**, 531–532 (2015).
8. Alberti, S. & Hyman, A. A. Insights & Perspectives Are aberrant phase transitions a driver of cellular aging? *BioEssays* **38**, 959–968 (2016).
9. Sleigh, J. N., Vagnoni, A., Twelvetrees, A. E. & Schiavo, G. Methodological advances in imaging intravital axonal transport. *F1000Research* **6**, 200 (2017).
10. Gumy, L. F. *et al.* Transcriptome analysis of embryonic and adult sensory axons reveals changes in mRNA repertoire localization. *RNA* **17**, 85–98

(2011).

11. Mellone, M. *et al.* Tau pathology is present in vivo and develops in vitro in sensory neurons from human P301S tau transgenic mice: a system for screening drugs against tauopathies. *J. Neurosci.* **33**, 18175–18189 (2013).

12. Stavoe, A. K., Gopal, P. P., Gubas, A., Tooze, S. A. & Holzbaur, E. L. Expression of WIPI2B counteracts age-related decline in autophagosome biogenesis in neurons. *Elife* **8**, e44219 (2019).

13. Klinman, E. & Holzbaur, E. L. F. Stress-Induced CDK5 Activation Disrupts Axonal Transport via Lis1/Ndel1/Dynein. *Cell Rep.* **12**, 462–473 (2015).

14. Pandey, J. P., Shi, L., Brebion, R. A. & Smith, D. S. LIS1 and NDEL1 Regulate Axonal Trafficking of Mitochondria in Mature Neurons. *Front. Mol. Neurosci.* **15**, 841047 (2022).

15. Lin, M.-Y. *et al.* Releasing Syntaphilin Removes Stressed Mitochondria from Axons Independent of Mitophagy under Pathophysiological Conditions. *Neuron* **94**, 595-610.e6 (2017).

16. Misgeld, T., Kerschensteiner, M., Bareyre, F. M., Burgess, R. W. & Lichtman, J. W. Imaging axonal transport of mitochondria in vivo. *Nat. Methods* **4**, 559–561 (2007).

17. Mitra, K. & Lippincott-Schwartz, J. Analysis of mitochondrial dynamics and functions using imaging approaches. *Curr. Protoc. Cell Biol.* **Chapter 4**, Unit 4.25.1–4.25.21 (2010).

18. van Spronsen, M. *et al.* TRAK/Milton motor-adaptor proteins steer mitochondrial trafficking to axons and dendrites. *Neuron* **77**, 485–502 (2013).

19. Chambers, J. E. *et al.* An Optical Technique for Mapping Microviscosity Dynamics in Cellular Organelles. *ACS Nano* **12**, 4398–4407 (2018).

20. Steinmark, I. E. *et al.* Targeted fluorescence lifetime probes reveal responsive organelle viscosity and membrane fluidity. *PLoS One* **14**, e0211165 (2019).

21. Guo, S. *et al.* Simultaneous monitoring of mitochondrial viscosity and membrane potential based on fluorescence changing and location switching of carbon dots in living cells. *Carbon N. Y.* **195**, 112–122 (2022).

22. Chen, Q. *et al.* A dual-labeling probe to track functional mitochondria–lysosome interactions in live cells. *Nat. Commun.* **11**, 6290 (2020).

23. Mecocci, P. *et al.* Mitochondrial membrane fluidity and oxidative damage to mitochondrial DNA in aged and AD human brain. *Mol. Chem. Neuropathol.* **31**, 53–64 (1997).

24. Kuter, K. *et al.* Adaptation within mitochondrial oxidative phosphorylation supercomplexes and membrane viscosity during degeneration of dopaminergic neurons in an animal model of early Parkinson's disease. *Biochim. Biophys. Acta - Mol. Basis Dis.* **1862**, 741–753 (2016).

25. Eckmann, J. *et al.* Mitochondrial Membrane Fluidity is Consistently Increased in Different Models of Huntington Disease: Restorative Effects of Olesoxime. *Mol. Neurobiol.* **50**, 107–118 (2014).

26. Brini, M. *et al.* A calcium signaling defect in the pathogenesis of a mitochondrial DNA inherited oxidative phosphorylation deficiency. *Nat. Med.* **5**, 951–954 (1999).

27. Duchen, M. R. Mitochondria and calcium: from cell signalling to cell death. *J. Physiol.* **529**, 57-68 (2000).

28. De vos, K. J. *et al.* VAPB interacts with the mitochondrial protein PTPIP51 to regulate calcium homeostasis. *Hum. Mol. Genet.* **21**, 1299-1311 (2012).

29. Molines, A. T. *et al.* Physical properties of the cytoplasm modulate the rates of

microtubule polymerization and depolymerization. *Dev. Cell* **57**, 466-479.e6 (2022).

30. Lee, T. H. & Linstedt, A. D. Osmotically Induced Cell Volume Changes Alter Anterograde and Retrograde Transport, Golgi Structure, and COPI Dissociation. *Mol. Biol. Cell* **10**, 1445–1462 (1999).

31. Nunes, P. *et al.* Ionic imbalance, in addition to molecular crowding, abates cytoskeletal dynamics and vesicle motility during hypertonic stress. *Proc. Natl. Acad. Sci. U. S. A.* **112**, E3104–E3113 (2015).

32. Clayton, A. H. A., Hanley, Q. S., Arndt-Jovin, D. J., Subramaniam, V. & Jovin, T. M. Dynamic fluorescence anisotropy imaging microscopy in the frequency domain (rFLIM). *Biophys. J.* **83**, 1631–1649 (2002).

33. Siegel, J. *et al.* Wide-field time-resolved fluorescence anisotropy imaging (TR-FAIM): Imaging the rotational mobility of a fluorophore. *Rev. Sci. Instrum.* **74**, 182–192 (2003).

34. Dix, J. A. & Verkman, A. S. Mapping of fluorescence anisotropy in living cells by ratio imaging. Application to cytoplasmic viscosity. *Biophys. J.* **57**, 231–240 (1990).

35. Miller, C. C. & Walker, J. The Stokes-Einstein law for diffusion in solution. *Proc. R. Soc. London. Ser. A, Contain. Pap. a Math. Phys. Character* **106**, 724–749 (1924).

36. Delarue, M. *et al.* mTORC1 Controls Phase Separation and the Biophysical Properties of the Cytoplasm by Tuning Crowding. *Cell* **174**, 338-349.e20 (2018).

37. Shu, T. *et al.* nucGEMs probe the biophysical properties of the nucleoplasm. *bioRxiv* 2021.11.18.469159 (2022) doi:10.1101/2021.11.18.469159.

38. Milde, S., Adalbert, R., Elaman, M. H. & Coleman, M. P. Axonal transport declines with age in two distinct phases separated by a period of relative stability. *Neurobiol. Aging* **36**, 971–981 (2015).

39. Mar, F. M. *et al.* CNS Axons Globally Increase Axonal Transport after Peripheral Conditioning. *J. Neurosci.* **34**, 5965–5970 (2014).

40. Sleigh, J. N., Rossor, A. M., Fellows, A. D., Tosolini, A. P. & Schiavo, G. Axonal transport and neurological disease. *Nat. Rev. Neurol*. **15** 691–703 (2019).

41. Berth, S. H. & Lloyd, T. E. Disruption of axonal transport in neurodegeneration. *J. Clin. Invest.* **133**, e168554 (2023).

42. Sun, N., Youle, R. J. & Finkel, T. The Mitochondrial Basis of Aging. *Mol. Cell* **61**, 654–666 (2016).

43. Sharma, A., Smith, H. J., Yao, P. & Mair, W. B. Causal roles of mitochondrial dynamics in longevity and healthy aging. *EMBO Rep.* **20**, e48395 (2019).

44. Stefanatos, R. & Sanz, A. The role of mitochondrial ROS in the aging brain. *FEBS Lett.* **592**, 743–758 (2018).

45. Markaki, M., Tsagkari, D. & Tavernarakis, N. Mitophagy and long-term neuronal homeostasis. *J. Cell Sci.* **136**, jcs260638 (2023).

46. Caponio, D. *et al.* Compromised autophagy and mitophagy in brain ageing and Alzheimer's diseases. *Aging Brain* **2**, 100056 (2022).

47. Rappe, A. & McWilliams, T. G. Mitophagy in the aging nervous system. *Front. Cell Dev. Biol.* **10**, 978142 (2022).

48. Kim, Y. *et al.* Mitochondrial Aging Defects Emerge in Directly Reprogrammed Human Neurons due to Their Metabolic Profile. *Cell Rep.* **23**, 2550–2558 (2018).

49. Miller, K. E. & Sheetz, M. P. Axonal mitochondrial transport and potential are correlated. *J. Cell Sci.* **117**, 2791–2804 (2004).

50. Sung, H., Tandarich, L. C., Nguyen, K. & Hollenbeck, P. J. Compartmentalized Regulation of Parkin-Mediated Mitochondrial Quality Control in the Drosophila Nervous System In Vivo. *J. Neurosci.* **36**, 7375–7391 (2016).

51. Baranov, S. V. *et al.* Mitochondria modulate programmed neuritic retraction. *Proc. Natl. Acad. Sci. U. S. A.* **116**, 650–659 (2019).

52. Hagemann, C. *et al.* Axonal Length Determines Distinct Homeostatic Phenotypes in Human iPSC Derived Motor Neurons on a Bioengineered Platform. *Adv. Healthc. Mater.* **11**, e2101817 (2022).

53. Persson, L. B., Ambati, V. S. & Brandman, O. Cellular Control of Viscosity Counters Changes in Temperature and Energy Availability. *Cell* **183**, 1572-1585.e16 (2020).

54. Puchkov, E. O. Intracellular viscosity: Methods of measurement and role in metabolism. *Biochem. Suppl. Ser. A Membr. Cell Biol.* **7**, 270–279 (2013).

55. Bulthuis, E. P. *et al.* Stress-dependent macromolecular crowding in the mitochondrial matrix. *EMBO J.* **42**, e108533 (2023).

56. Koopman, W. J. H. *et al.* Inherited complex I deficiency is associated with faster protein diffusion in the matrix of moving mitochondria. *Am. J. Physiol. Physiol.* **294**, C1124–C1132 (2008).

57. Fecher, C. *et al.* Cell-type-specific profiling of brain mitochondria reveals functional and molecular diversity. *Nat. Neurosci.* **22**, 1731–1742 (2019).

58. Faitg, J. *et al.* 3D neuronal mitochondrial morphology in axons, dendrites, and somata of the aging mouse hippocampus. *Cell Rep.* **36**, 109509 (2021).

59. MacAskill, A. F. *et al.* Miro1 Is a Calcium Sensor for Glutamate Receptor-

Dependent Localization of Mitochondria at Synapses. *Neuron* **61**, 541–555 (2009).

60. Wang, X. & Schwarz, T. L. The Mechanism of Ca2+-Dependent Regulation of Kinesin-Mediated Mitochondrial Motility. *Cell* **136**, 163–174 (2009).

61. Chang, K. T., Niescier, R. F. & Min, K.-T. Mitochondrial matrix Ca2+ as an intrinsic signal regulating mitochondrial motility in axons. *Proc. Natl. Acad. Sci. U. S. A.* **108**, 15456–15461 (2011).

62. Niescier, R. F., Hong, K., Park, D. & Min, K. T. MCU Interacts with Miro1 to Modulate Mitochondrial Functions in Neurons. *J. Neurosci.* **38**, 4666–4677 (2018).

63. Metzner, K. *et al.* Age-dependent increase of cytoskeletal components in sensory axons in human skin. *Front. Cell Dev. Biol.* **10**, (2022).

64. Leduc, C. *et al.* Molecular crowding creates traffic jams of kinesin motors on microtubules. *Proc. Natl. Acad. Sci.* **109**, 6100–6105 (2012).

65. Sabharwal, V. & Koushika, S. P. Crowd Control: Effects of Physical Crowding on Cargo Movement in Healthy and Diseased Neurons. *Front. Cell. Neurosci.* **13**, (2019).

66. Sood, P. *et al.* Cargo crowding at actin-rich regions along axons causes local traffic jams. *Traffic* **19**, 166–181 (2018).

67. Parry, B. R., Surovtsev, I. V, Cabeen, M. T., Hern, C. S. O. & Dufresne, E. R. The Bacterial Cytoplasm Has Glass-like Properties and Is Fluidized by Metabolic Activity. *Cell* **156**, 183–194 (2014).

68. Kubánková, M., Summers, P. A., López-Duarte, I., Kiryushko, D. & Kuimova, M. K. Microscopic Viscosity of Neuronal Plasma Membranes Measured Using Fluorescent Molecular Rotors: Effects of Oxidative Stress and

Neuroprotection. *ACS Appl. Mater. Interfaces* **11**, 36307–36315 (2019).

69. Sugawa, M. *et al.* Impaired Plasticity of Neurons in Aging. *Ann. N. Y. Acad. Sci.* **786**, 274–282 (1996).

70. Lamoureux, P. L., O'Toole, M. R., Heidemann, S. R. & Miller, K. E. Slowing of axonal regeneration is correlated with increased axonal viscosity during aging. *BMC Neurosci.* **11**, 140 (2010).

71. Zustiak, S. P., Nossal, R. & Sackett, D. L. Hindered Diffusion in Polymeric Solutions Studied by Fluorescence Correlation Spectroscopy. *Biophys. J.* **101**, 255–264 (2011).

72. Sleigh, J. N., Weir, G. A. & Schiavo, G. A simple , step - by - step dissection protocol for the rapid isolation of mouse dorsal root ganglia. *BMC Res. Notes* **9**, 82 (2016).

73. Sleigh, J. N. *et al.* Trk receptor signaling and sensory neuron fate are perturbed in human neuropathy caused by Gars mutations. *Proc. Natl. Acad. Sci. U. S. A.* **114**, E3324–E3333 (2017).

74. Mattedi, F., Lloyd-Morris, E., Hirth, F. & Vagnoni, A. Optogenetic cleavage of the Miro GTPase reveals the direct consequences of real-time loss of function in Drosophila. *PLoS Biol.* **21**, e3002273 (2023).

75. Annuario, E., Ng, K. & Vagnoni, A. High-Resolution Imaging of Mitochondria and Mitochondrial Nucleoids in Differentiated SH-SY5Y Cells. *Methods Mol. Biol.* **2431**, 291–310 (2022).

76. Sleigh, J. N., Tosolini, A. P. & Schiavo, G. In vivo imaging of anterograde and retrograde axonal transport in rodent peripheral nerves. *Methods Mol. Biol.* **2143**, 271–292 (2020).

77. Tosolini, A. P., Villarroel-Campos, D., Schiavo, G. & Sleigh, J. N. Expanding

the Toolkit for In Vivo Imaging of Axonal Transport. *J. Vis. Exp.* **178** (2021).

78. Lidke, K. A., Rieger, B., Lidke, D. S. & Jovin, T. M. The role of photon statistics in fluorescence anisotropy imaging. *IEEE Trans. image Process.* **14**, 1237–1245 (2005).

79. Verkman, A. S., Armijo, M. & Fushimi, K. Construction and evaluation of a frequency-domain epifluorescence microscope for lifetime and anisotropy decay measurements in subcellular domains. *Biophys. Chem.* **40**, 117–125 (1991).